NORTHWESTERN UNIVERSITY

Parameter Estimation Using Markov Chain Monte Carlo Methods for Gravitational Waves from Spinning Inspirals of Compact Objects

A DISSERTATION

SUBMITTED TO THE GRADUATE SCHOOL
IN PARTIAL FULFILLMENT OF THE REQUIREMENTS

for the degree

DOCTOR OF PHILOSOPHY

Field of Physics and Astronomy

By

Vivien Raymond

EVANSTON, ILLINOIS

June 2012

ABSTRACT

Parameter Estimation Using Markov Chain Monte Carlo Methods for Gravitational Waves from Spinning Inspirals of Compact Objects

Vivien Raymond

Gravitational waves are on the verge of opening a brand new window on the Universe. However, gravitational wave astronomy comes with very unique challenges in data analysis and signal processing in order to lead to new discoveries in astrophysics. Among the sources of gravitational waves, inspiraling binary systems of compact objects, neutron stars and/or black holes in the mass range $1\,\mathrm{M}_\odot$ - $100\,\mathrm{M}_\odot$ stand out as likely to be detected and relatively easy to model.

The detection of a gravitational wave event is challenging and will be a rewarding achievement by itself. After such a detection, measurement of source properties holds major promise for improving our astrophysical understanding and requires reliable methods for parameter estimation and model selection. This is a complicated problem, because of the large number of parameters (15 for spinning compact objects in a quasi-circular orbit) and the degeneracies between them, the significant amount of structure in the parameter space, and the particularities of the detector noise.

This work presents the development of a parameter-estimation and model-selection algorithm, based on Bayesian statistical theory and using Markov chain Monte Carlo methods for ground-based gravitational-wave detectors (LIGO and Virgo). This method started from existing non-spinning and single spin stand-alone analysis codes and was developed into a method able to tackle the complexity of fully spinning systems, and infer all spinning parameters of a compact binary. Not only are spinning parameters believed to be astrophysically significant, but this work has shown that not including them in the analysis can lead to biases in parameter recovery.

This work made it possible to answer several scientific questions involving parameter estimation of inspiraling spinning compact objects, which are addressed in the chapters of this dissertation.

Acknowledgements

First and foremost, I want to thank my advisor, Professor Vicky Kalogera, for everything. She gave me a great research project, as well as help and advice in more ways than I thought possible. There is no doubt that my graduate school experience was successful thanks to her. I also want to thank the following people, in no particular order: all my colleagues in gravitational-wave astronomy at Northwestern University; Marc van der Sluys who was patient enough to educate a beginner; Ilya Mandel who kept teaching me new things; Ben Farr who became a great colleague; Will Farr for all his help, and who I know will become an amazing professor; and all the people not named here, who are also responsible for making my PhD possible. I cannot name all the people I am grateful to, but special thanks to: all the graduate students, post-docs, and faculty members who made Dearborn Observatory such a great place to work and study, including during those 28-hour workdays; all the members of Parameter Estimation group, the Compact Binary Coalescence group and the LIGO-Virgo Collaboration who provided a lot of extremely time-saving help (and made it a great thing to work in a 1000+ members international collaboration); all my friends who helped me, managed to survive all my complaining, and made Chicago's 14-month winter easy to forget; and especially my family - Mom, Dad, and Charline, thanks for all the support!

I would also like to gratefully acknowledge the support of the United States National Science Foundation for the construction and operation of the LIGO Laboratory, the Science and Technology Facilities Council of the United Kingdom, the Max-Planck-Society, and the State of Niedersachsen/Germany for support of the construction and operation of the GEO600 detector, and the Italian Istituto Nazionale di Fisica Nucleare and the French Centre National de la Recherche Scientifique for the construction and operation of the Virgo detector. I also gratefully acknowledge the support of the research by these agencies and by the Australian Research Council, the International Science Linkages program of the Commonwealth of Australia, the Council of Scientific and Industrial Research of India, the Istituto Nazionale di Fisica Nucleare of Italy, the Spanish Ministerio de Economía y Competitividad, the Conselleria d'Economia Hisenda i Innovació of the Govern de les Illes Balears, the Foundation for Fundamental Research on Matter supported by the Netherlands Organisation for Scientific Research, the Polish Ministry of Science and Higher Education, the FOCUS Programme of Foundation for Polish Science, the Royal Society, the Scottish Funding Council, the Scottish Universities Physics Alliance, The National Aeronautics and Space Administration, the Carnegie Trust, the Leverhulme Trust, the David and Lucile Packard Foundation, the Research Corporation, and the Alfred P. Sloan Foundation.

Table of Contents

List of Tables

List of Figures

CHAPTER 1

Introduction

This work does not reflect the scientific opinion of the LIGO Scientific Collaboration and it was not reviewed by the collaboration. The results are under LIGO Scientific Collaboration review and potentially subject to change.

1.1. Statement of the problem

Gravitational waves from coalescing compact binaries, a likely source for ground-based gravitational-wave detectors, encode information about source physics. Detailed models of the anticipated waveforms from these coalescences enable inference on parameters including component masses, spins, sky location, and distance. Parameter estimation and model selection in multi-dimensional parameter spaces are complex but necessary in order to pursue gravitational-wave astronomy and astrophysics. The main goal of this dissertation is to provide an inference method for gravitational waves from spinning compact binary coalescences as an improvement over the existing non-spinning methods. Using this newly developed tool, the potentially significant biases from ignoring spinning effects are shown and the measurability of spinning models and spinning parameter is discussed.

1.2. Motivation and Methodology

Gravitational waves are a prediction from General Relativity [1, 2] and have been indirectly observed in the Hulse-Taylor pulsar [3]. Their direct observation has tremendous potential in constraining stellar models, testing gravity in the strong field regime for the first time, measuring the equation of state of matter at densities unattainable in laboratories and even observing phenomena where the two incompatible great theories of modern physics, general relativity and quantum mechanics, are valid.

Among the sources of gravitational waves (GWs), inspiralling binary systems of compact objects, neutron stars (NSs) and/or black holes (BHs) in the mass range $\sim 1\,\mathrm{M}_\odot - 100\,\mathrm{M}_\odot$ stand out as likely to be detected and relatively easy to model. For current first-generation ground-based laser interferometers [4], LIGO (Laser Interferometer Gravitational-wave Observatory) [5] and Virgo [6], the detection-rate estimates for compact object binaries range from $4.7 * 10^{-4}$ to $0.8\,yr^{-1}$ [7]. Although the estimates are quite uncertain, detection rates are expected to increase with the upgrade to Advanced LIGO/Virgo to about $70yr^{-1}$.

The detection of a gravitational-wave event is challenging and will be a rewarding achievement by itself. After such a detection, measurement of source properties holds major promise for improving our astrophysical understanding and requires reliable methods for parameter estimation. This is a complicated problem because of the large number of parameters (15 for spinning compact objects in a quasi-circular orbit) and the degeneracies between them [8], the significant amount of structure in the parameter space, and the particularities of the detector noise.

The parameter estimation of signals using non-spinning models is much easier and has been accomplished, [9, 10, 11, 12, 13] but it provides potentially significant biases on spinning sources which are believed to be astrophysically significant [14]. Including spins adds 6 parameters (2 spin vectors) to originally 9 non-spinning parameters. However, more relevant to data analysis difficulties, the change adds 6 intrinsic parameters to a problem containing only 2 (the masses of the binary), while transforming another parameter (inclination) from separable to intrinsically linked to the evolution of the binary system and the production of gravitational waves. Additional correlations and degeneracy are also introduced (spin magnitudes and masses), while at the same time potentially helping to differentiate between near degenerate modes [8].

The increased complexity required developing specific methods for exploring the spinning parameter space in the case of LIGO-Virgo data from existing non-spinning [10, 15] and single spin [16] stand-alone analysis codes. I use the Markov chain Monte Carlo (MCMC) [17] algorithm in this Bayesian inference method to produce the complete probability density function (PDF) of the parameter set of the model used to match the data. In addition, Bayes factors measuring the probability of one model versus another model fitting the data can be obtained.

1.2.1. Gravitational waves

I give in this section a limited introduction to gravitational waves as they emerge from general relativity. For a more detailed description, see for instance [18]. General relativity introduces the concept of a space-time curved by the presence of mass, energy and momentum.

In the following, the Einstein notation will be used, in which repeated vector indices (v^α) and covector indices (c_α) imply a summation, i.e. $c_\alpha v^\alpha = \sum_{\alpha=0}^{3} c_\alpha v^\alpha$. Space-time is described by the metric tensor $g_{\alpha\beta}$, as in for instance the metric tensor of flat space-time (where c is the speed of light in vacuum):

$$\eta_{\alpha\beta}(x) = \begin{pmatrix} -1/c & 0 & 0 & 0 \\ 0 & 1 & 0 & 0 \\ 0 & 0 & 1 & 0 \\ 0 & 0 & 0 & 1 \end{pmatrix} \tag{1.1}$$

From the metric $g_{\alpha\beta}$ one can construct the Christoffel symbols:

$$\Gamma^{\delta}_{\alpha\beta} = g^{\delta\gamma}\frac{1}{2}(\partial_\beta g_{\gamma\alpha} + \partial_\alpha g_{\gamma\beta} - \partial_\gamma g_{\alpha\beta}) \tag{1.2}$$

and the Riemann curvature tensor $R^{\rho}_{\sigma\mu\nu}$:

$$R^{\rho}_{\sigma\mu\nu} = \partial_\mu \Gamma^{\rho}_{\nu\sigma} - \partial_\nu \Gamma^{\rho}_{\mu\sigma} + \Gamma^{\rho}_{\mu\gamma}\Gamma^{\gamma}_{\nu\sigma} - \Gamma^{\rho}_{\nu\gamma}\Gamma^{\gamma}_{\mu\sigma} \tag{1.3}$$

which can be contracted to define the Ricci curvature tensor $R_{\alpha\beta}$:

$$R_{\alpha\beta} = R^{\delta}_{\alpha\delta\beta} \tag{1.4}$$

and yields the Einstein tensor $G_{\alpha\beta}$:

$$G_{\alpha\beta} = R_{\alpha\beta} - \frac{1}{2}R_{\alpha\beta} \tag{1.5}$$

Starting from the Einstein equation in vacuum:

$$G_{\alpha\beta} = 0 \tag{1.6}$$

we write a small perturbation of the metric of flat spacetime:

$$g_{\alpha\beta}(x) = \eta_{\alpha\beta} + h_{\alpha\beta}(x) \tag{1.7}$$

To first order in the perturbation $||h_{\alpha\beta}(x)|| \ll 1$, using the gauge condition:

$$\left(\partial_\beta h^\beta_\alpha(x) - \tfrac{1}{2}\partial_\alpha h^\beta_\beta(x) = 0\right) \tag{1.8}$$

the Einstein equation in vacuum becomes:

$$\Box\, h_{\alpha\beta} = 0 \tag{1.9}$$

where $\Box \equiv -\partial^2/\partial(ct)^2 + \nabla^2$ is the flat-spacetime wave operator.

Equation 1.9 is a wave equation, and the resulting wave solution travels at the speed of light, is transverse, and has two polarisations:

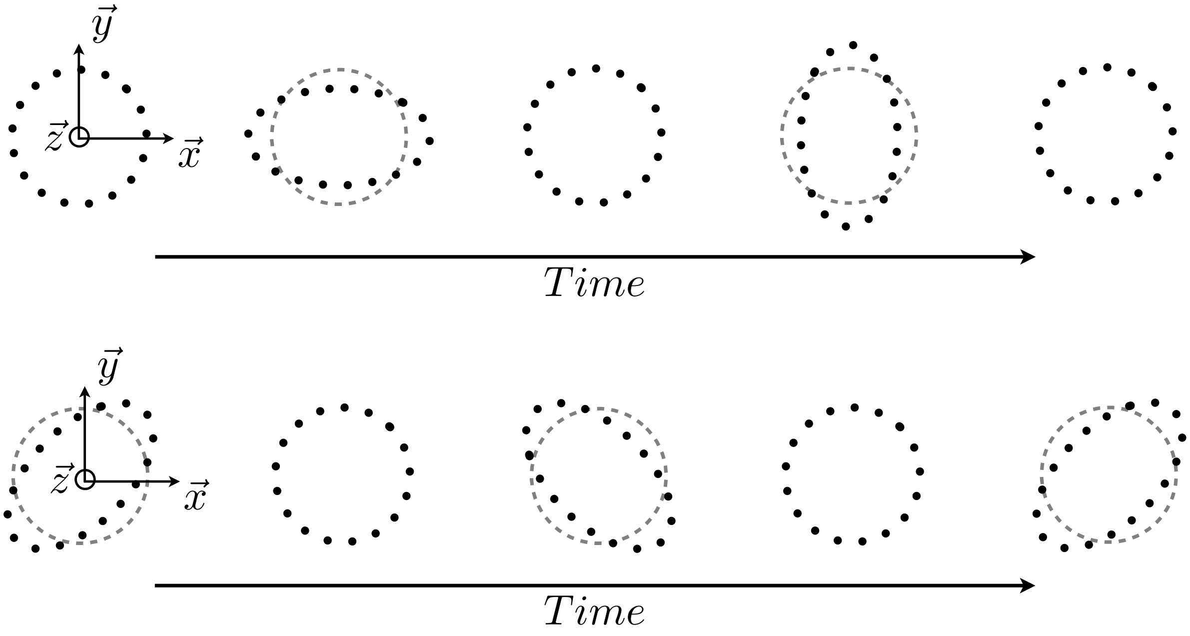

Figure 1.1. Illustration of the effect a gravitational wave would have on a ring of free falling test masses. For a wave propagating perpendicularly to the plane in which the ring is arranged, the plus (+, top row) and cross (×, bottom row) polarizations stretch and squeeze the ring in two patterns related by a $\pi/4$ rotation.

$$h_{\alpha\beta}(x) = \begin{pmatrix} 0 & 0 & 0 & 0 \\ 0 & h_+ & h_\times & 0 \\ 0 & h_\times & -h_+ & 0 \\ 0 & 0 & 0 & 0 \end{pmatrix} \tag{1.10}$$

The effect such a wave has on a ring of free falling test masses is illustrated in Fig. 1.1.

The gravitational force is much weaker than the other three fundamental forces, and as such couples weakly with matter. This means on the one hand that they propagate through the universe easily, and on the other hand that they interact weakly with a detector. See Section 1.2.3 for magnitude estimates. In a ground-based interferometer like the LIGO [5] or Virgo [6] observatories, the free falling masses are replaced with two suspended mirrors at the end of the x- and y-axes of Fig. 1.1. A laser beam is shone from the origin onto both mirrors to form a Michelson interferometer which measures the stretching and squeezing along the x and y axes. An observatory set up this way is sensitive to

$$h(t) = \tfrac{1}{2}(h^d_{xx} - h^d_{yy}) = F_+ \, h_+ \; + \; F_\times \, h_\times \tag{1.11}$$

Where F_+ and $F_\times$ are the antenna beam patterns of the detector, relating the coordinate system of the detector to the coordinate system of gravitational-wave source. $F_{+,\times}(\alpha, \delta, \psi)$ are functions of the hour-angle α (right ascension corrected for the earth's rotation), the declination δ and polarisation angle ψ of the source. They are also parameterised by the time at geocentre t_c and the detector's three dimensional 2nd-order response tensor D (which relates the local coordinates of the detector to the geocentric reference system where α,δ and ψ are defined).

$$F_+(\alpha, \delta, \psi) = X^T(\alpha, \delta, \psi) \cdot D \cdot X(\alpha, \delta, \psi) - Y^T(\alpha, \delta, \psi) \cdot D \cdot Y(\alpha, \delta, \psi) \tag{1.12}$$

$$F_\times(\alpha, \delta, \psi) = X^T(\alpha, \delta, \psi) \cdot D \cdot Y(\alpha, \delta, \psi) + Y^T(\alpha, \delta, \psi) \cdot D \cdot X(\alpha, \delta, \psi) \tag{1.13}$$

Where the vectors $X(\alpha, \delta, \psi)$ and $Y(\alpha, \delta, \psi)$ are:

$$X(\alpha,\delta,\psi) = \begin{pmatrix} -\cos\psi\,\sin\alpha - \sin\psi\,\cos\alpha\,\sin\delta \\ -\cos\psi\,\cos\alpha + \sin\psi\,\sin\alpha\,\sin\delta \\ \sin\psi\,\cos\delta \end{pmatrix} \tag{1.14}$$

$$Y(\alpha,\delta,\psi) = \begin{pmatrix} \sin\psi\,\sin\alpha - \cos\psi\,\cos\alpha\,\sin\delta \\ \sin\psi\,\cos\alpha + \cos\psi\,\sin\alpha\,\sin\delta \\ \cos\psi\,\cos\delta \end{pmatrix} \tag{1.15}$$

In the presence of matter, Eq. 1.6 becomes:

$$G_{\alpha\beta} = 8\pi(G/c^4)T_{\alpha\beta} \tag{1.16}$$

Where $T_{\alpha\beta}$ is the stress-energy-momentum tensor, generalizing the stress tensor of Newtonian physics. G is the gravitational constant. And Eq. 1.9 becomes the "relaxed" Einstein equation:

$$\Box h^{\alpha\beta} = -16\pi(G/c^4)\tau^{\alpha\beta}, \tag{1.17}$$

Where $\tau^{\alpha\beta}$ is the"effective" energy-momentum pseudotensor:

$$\tau^{\alpha\beta} = (-||g_{\alpha\beta}||)T^{\alpha\beta} + (16\pi)^{-1}\Lambda^{\alpha\beta}, \tag{1.18}$$

and $\Lambda^{\alpha\beta}$ is the non-linear "field" contribution given by terms quadratic (and higher) in $h^{\alpha\beta}$ and its derivatives

1.2.2. Post-Newtonian Expansion

The post-Newtonian (pN) approximation is an expansion of the Einstein equation in powers of $(v/c)^2$ where v denotes the characteristic velocity of the system and c is the speed of light in vacuum.

Eq. 1.17 is called "relaxed" because it can be solved formally as a functional of source variables without specifying the motion of the source, in the form

$$h^{\alpha\beta}(t,\mathbf{x}) = \frac{4G}{c^4}\int_{\mathcal{C}} \frac{\tau^{\alpha\beta}(t-|\mathbf{x}-\mathbf{x}'|/c,\mathbf{x}')}{|\mathbf{x}-\mathbf{x}'|} d^3x', \tag{1.19}$$

where the integration is over the past flat-spacetime null cone $\mathcal{C}$ of the field point $(t,\mathbf{x})$. The motion of the source is then determined from the covariant equation of motion $\nabla_\beta T^{\alpha\beta} = 0$. This formal solution can then be iterated in the weak-field ($||h^{\alpha\beta}|| \ll 1$) approximation. First comes the substitution of $h_0^{\alpha\beta} = 0$ into the source $\tau^{\alpha\beta}$ in Eq. (1.19), and then solving for the first iteration $h_1^{\alpha\beta}$. Then one repeats the procedure sufficiently many times to achieve a solution of the desired accuracy. Post-Newtonian theory comes from imposing the additional slow motion assumption ($v \ll c$).

Among the results of this approach are formulae for the equations of motion and gravitational waveform of binary systems of compact objects, carried out to high orders in a post-Newtonian expansion. For example, the relative two-body equation of motion has the form

$$\begin{aligned}\frac{d\mathbf{v}}{dt} &= \frac{Gm}{r^2}\biggl\{-\hat{\mathbf{n}} + \frac{1}{c^2}\mathbf{A}_{\text{1pN}} + \frac{1}{c^4}\mathbf{A}_{\text{2pN}} + \frac{1}{c^5}\mathbf{A}_{\text{2.5pN}} \\ &\qquad + \frac{1}{c^6}\mathbf{A}_{\text{3pN}} + \frac{1}{c^7}\mathbf{A}_{\text{3.5pN}} + \dots\biggr\}, \end{aligned} \tag{1.20}$$

where $m = m_1 + m_2$ is the total mass, $r = |\mathbf{x}_1 - \mathbf{x}_2|$, $\mathbf{v} = \mathbf{v}_1 - \mathbf{v}_2$, and $\hat{\mathbf{n}} = (\mathbf{x}_1 - \mathbf{x}_2)/r$. The notation $\mathbf{A}_{n\text{pN}}$ indicates that the term is $O(\epsilon^n)$ relative to the leading Newtonian term $-\hat{\mathbf{n}}$. However, the post-Newtonian series has not been proven to formally converge. Explicit formulae for non-spinning bodies through 3.5pN order have been calculated, and a number of spin-orbit and spin-spin contributions have been obtained up to 2.5pN order (see [19] for a review).

Another product is a formula for the gravitational field far from the system, whose spatial components $h^{\alpha\beta}$ are used as templates in gravitational-wave data analysis.

$$\begin{aligned}h^{\alpha\beta}(t,\mathbf{x}) &= \frac{2Gm}{dc^4}\biggl\{Q^{\alpha\beta} + \frac{1}{c}Q^{\alpha\beta}_{\text{0.5pN}} + \frac{1}{c^2}Q^{\alpha\beta}_{\text{1pN}} + \frac{1}{c^3}Q^{\alpha\beta}_{\text{1.5pN}} \\ &\qquad + \frac{1}{c^4}Q^{\alpha\beta}_{\text{2pN}} + \frac{1}{c^5}Q^{\alpha\beta}_{\text{2.5pN}} + \dots\biggr\}, \end{aligned} \tag{1.21}$$

where d is the distance from the source, and the variables are to be evaluated at retarded time $t - d/c$. Here $\{t, \mathbf{x}\} = x$. The leading term is the so-called quadrupole formula, given explicitly by

$$h^{\alpha\beta}(t,\mathbf{x}) = \frac{2G}{dc^4}\ddot{I}^{\alpha\beta}(t - d/c)\,, \tag{1.22}$$

where $I^{\alpha\beta}$ is the quadrupole moment of the source, and overdots denote time derivatives.

1.2.3. Compact Binary Coalescence

From Eq. 1.22, we see that in order to produce gravitational waves, the source needs to have a time-varying quadrupole moment. One of the promising sources of gravitational waves is the coalescence of two compact objects. In order to get an order-of-magnitude estimate of the amplitude of gravitational wave from such a system, lets assume that both compact objects have mass M, and each are moving about the centre of mass in a circular orbit of period P and radius R. We then get for the quadrupole moment:

$$\begin{aligned} I^{\alpha\beta} &\approx MR^2 \\ \ddot{I}^{\alpha\beta} &\approx \frac{MR^2}{P^2} \end{aligned} \tag{1.23}$$

From Newtonian dynamics we have:

$$\frac{(2\pi R/P)^2}{R} = \frac{M}{(2R^2)} \tag{1.24}$$

And from Eq. 1.22 we can estimate:

$$||h^{\alpha\beta}(t, \mathbf{x})|| \approx M^{5/3}P^{-2/3}d^{-1} \tag{1.25}$$

And with some astrophysically relevant units:

$$||h^{\alpha\beta}(t,\mathbf{x})|| \approx 10^{-21} \left(\frac{M}{10\,\mathrm{M}_\odot}\right)^{5/3} \left(\frac{1\,\mathrm{s}}{P}\right)^{2/3} \left(\frac{1\,\mathrm{Mpc}}{d}\right) \tag{1.26}$$

Which leads to a typical displacement of one part in 10^{21}.

For a binary system Eq. 1.22 leads to $Q^{\alpha\beta} = 2\eta(v^i v^j - Gm\hat{n}^i\hat{n}^j/r)$. Where $\eta = \frac{M_1 M_2}{(M_1+M_2)^2}$ is the symmetric mass ratio. For binary systems, explicit formulae for the waveform through 3.5pN order have been derived (see [19] for a full review).

With the gravitational waveform, one can compute the rate at which energy is carried off by the radiation. The lowest-order quadrupole formula leads to the gravitational wave energy flux

$$\dot{E} = \frac{8}{15}\eta^2 \frac{G^2 m^4}{r^4 c^5}(12v^2 - 11\dot{r}^2). \tag{1.27}$$

This has been extended to 3.5pN order beyond the quadrupole formula [19]. Formulae for fluxes of angular and linear momentum can also be derived. The 2.5pN radiation-reaction terms in the equation of motion (1.20) result in a decrease of the orbital energy at a rate that precisely balances the energy flux (1.27) determined from the waveform. Averaged over one orbit, this results in a rate of increase of the binary's orbital frequency given by

$$\frac{df_\mathrm{b}}{dt} = \frac{192\pi}{5} f_\mathrm{b}^2 \left(\frac{2\pi G\mathcal{M} f_\mathrm{b}}{c^3}\right)^{5/3} F(e) \tag{1.28}$$

where

$$F(e) = (1-e^2)^{-7/2}\left(1 + \frac{73}{24}e^2 + \frac{37}{96}e^4\right), \tag{1.29}$$

and $\mathcal{M} = \frac{(M_1 M_2)^{3/5}}{(M_1+M_2)^{1/5}}$ is the chirp mass. By making precise measurements of the phase $\Phi(t) = 2\pi \int^t f(t')dt'$ of the gravitational waves (for which $f = 2f_{\rm b}$ for the dominant component) as a function of the frequency, one can measures the chirp mass of the system. Using templates including higher order in the phase allows for more parameters to be measured.

A circular binary inspiral with both compact objects spinning is described by a 15-dimensional parameter vector $\vec{\lambda} \in \Lambda$. A possible choice of independent parameters with respect to a fixed geocentric coordinate system is:

$$\vec{\lambda} = \{\mathcal{M}, \eta, d_{\rm L}, t_{\rm c}, \phi_{\rm c}, \alpha, \delta, \iota, \psi, a_{\rm spin1}, \theta_{\rm spin1}, \phi_{\rm spin1}, a_{\rm spin2}, \theta_{\rm spin2}, \phi_{\rm spin2}\} \tag{1.30}$$

where $\mathcal{M}$ and η are the chirp mass and symmetric mass ratio, respectively; $d_{\rm L}$ is the luminosity distance to the source; $\phi_{\rm c}$ is an integration constant that specifies the gravitational-wave phase at the time of coalescence $t_{\rm c}$, defined with respect to the centre of the Earth; α (right ascension) and δ (declination) identify the source position in the sky; ι defines the inclination of the binary with respect to the line of sight; and ψ is the polarisation angle of the waveform. The spins are specified by $0 \leq a_{{\rm spin}_{1,2}} \equiv S_{1,2}/M_{1,2}^2 \leq 1$ as the dimensionless spin magnitude, and the angles $\theta_{\rm spin1,2}$,$\phi_{\rm spin1,2}$ for their orientations.

It is convenient to define two families of parameters. The intrinsic parameters:

$$\overrightarrow{\lambda_{intrinsic}} = \{\mathcal{M}, \eta, a_{\rm spin1}, \theta_{\rm spin1}, \phi_{\rm spin1}, a_{\rm spin2}, \theta_{\rm spin2}, \phi_{\rm spin2}\} \tag{1.31}$$

are intrinsically linked to the computation of the gravitational wave in any reference frame. While the extrinsic parameters:

$$\overrightarrow{\lambda_{extrinsic}} = \{d_\mathrm{L}, t_\mathrm{c}, \phi_\mathrm{c}, \alpha, \delta, \iota, \psi\} \tag{1.32}$$

control the projection of the gravitational wave onto the geocentric reference frame, in which we can compute the response of each detector with Eq. 1.13. The parameter space is significantly smoother in the extrinsic variables than the intrinsic ones. This leads to increased difficulty in tackling the spinning parameter estimation problem beyond the increase in dimensionality. The intrinsic parameters space goes from two dimensions to eight, and inclination of the orbital plane is not constant anymore, causing the transformation from the source frame to the geocentric frame to be time-varying.

This qualitative difference between spinning and non-spinning leads to potential systematic biases in parameter recovery when not including spin in the analysis. For instance the mass ratio as shown in an example in Section 2.3.3. In addition spin is believed to be astrophically significant, see [14]. The classical stellar evolution scenario to form compact objects binaries is believed to be the main sources of gravitational wave for LIGO-Virgo and its upgrade, Advanced LIGO-Virgo, from [7]:

Table 1.1. Detection rates for compact binary coalescence sources.

IFO	Source	N_{low} yr^{-1}	$N_{realistic}$ yr^{-1}	N_{high} yr^{-1}	$N_{upperlimit}$ yr^{-1}
Initial	NS-NS	2×10^{-4}	0.02	0.2	0.6
	NS-BH	7×10^{-5}	0.004	0.1	
	BH-BH	2×10^{-4}	0.007	0.5	
Advanced	NS-NS	0.4	40	400	1000
	NS-BH	0.2	10	300	
	BH-BH	0.4	20	1000	

In this formation scenario, in very broad terms, a binary star evolves until the primary member explodes as a supernova and leaves a spinning compact object around which a star orbits. By the time the second star explodes, any misalignment between the spin of the first compact object and the orbit should have decayed away due to mass transfer between the binary components. Such mass transfer can also spin up further the first compact object. With the second supernova, a second spinning compact object is formed. Furthermore the supernova kick imparted to the second compact object does not just alter the orbital size and eccentricity, but it can also tilt the orbital plane, leading to a misalignment developing between the compact objects' spins and the orbital angular momentum. Since at this state the binary consists of two compact objects and hence no subsequent mass transfer and spin alignment is possible. An alternative formation scenario involving dynamical interaction in dense stellar environment (for instance globular clusters) is also considered by the astrophysical community (see [**20**]). In this case, spin orientations are believed to be random. In addition, misaligned spins are not believed to significantly align due to gravitational radiations [**21**].

1.2.4. Bayesian framework and signal processing

The aim of this analysis is to determine the multi-dimensional *posterior* probability-density function of the unknown parameter vector $\vec{\lambda}$ in equation 1.30, given the data sets x_a collected by a network of n_{det} detectors, a model M of the waveform and the *prior* $p(\vec{\lambda})$ on the parameters. Our priors are uniform in the parameters of Eq. 5.1 (see [**16**] for details). One can compute the probability density via Bayes' theorem

$$p(\vec{\lambda}|x_a, M) = \frac{p(\vec{\lambda}|M)\, p(x_a|\vec{\lambda}, M)}{p(x_a|M)}\,, \tag{1.33}$$

where

$$\mathcal{L} \equiv p(x_a|\vec{\lambda}, M) \propto \exp\left(< x_a|h_a(\vec{\lambda}) > -\frac{1}{2} < h_a(\vec{\lambda})|h_a(\vec{\lambda}) >\right) \tag{1.34}$$

is the *likelihood function*, which measures how well the data fits the model M for the parameter vector $\vec{\lambda}$. The term $p(x_a|M)$ is the *marginal likelihood* or *evidence*. In the previous equation

$$< x|y >= 4Re\left(\int_{f_{\rm low}}^{f_{\rm high}} \frac{\tilde{x}(f)\tilde{y}^*(f)}{S_a(f)}\,{\rm d}f\right) \tag{1.35}$$

is the *overlap* of signals x and y, $\tilde{x}(f)$ is the Fourier transform of $x(t)$, and $S_a(f)$ is the noise power-spectral density in detector a. For future reference, I also define match between two waveforms corresponding to different parameter values as the overlap between the normalised waveforms:

$$M(h(\vec{\lambda_1}), h(\vec{\lambda_2})) = \frac{< h(\vec{\lambda_1})|h(\vec{\lambda_2}) >}{\sqrt{< h(\vec{\lambda_1})|h(\vec{\lambda_1}) >< h(\vec{\lambda_2})|h(\vec{\lambda_2}) >}} \tag{1.36}$$

The likelihood computed for the injection parameters $\mathcal{L}_{\rm inj} = p(x_a|\vec{\lambda}_{\rm inj}, M)$ is then a random variable that depends on the particular noise realisation n_a in the data $x_a = h(\vec{\lambda}_{\rm inj}) + n_a$. The injection parameters are the parameters of the waveform template added to the noise.

I define the signal-to-noise ratio (SNR) of the injection to be:

$$\text{SNR} = \frac{< x|h(\vec{\lambda}_{\text{inj}}) >}{\sqrt{< h(\vec{\lambda}_{\text{inj}})|h(\vec{\lambda}_{\text{inj}}) >}}. \tag{1.37}$$

From here on, I use the expected value of the signal-to-noise ratio, which is equal to the square root of twice the expectation value of $\log \mathcal{L}_{\text{inj}}$:

$$\text{SNR} = \sqrt{< h(\vec{\lambda}_{\text{inj}})|h(\vec{\lambda}_{\text{inj}}) >}. \tag{1.38}$$

To combine observations from a network of detectors with uncorrelated noise realisations we have the likelihood $p(\vec{x}|\vec{\lambda}, M) = \prod_{a=1}^{n_{\text{det}}} p(x_a|\vec{\lambda}, M)$, for $\vec{x} \equiv \{x_a : a = 1, \ldots, n_{\text{det}}\}$ and

$$p(\vec{\lambda}|\vec{x}, M) = \frac{p(\vec{\lambda}|M)\, p(\vec{x}|\vec{\lambda}, M)}{p(\vec{x}|M)}. \tag{1.39}$$

The numerical computation of the probability-density function involves the evaluation of a large multi-modal, multi-dimensional integral. Markov chain Monte Carlo methods, *e.g.* [**17**, **22**] and references therein, have proved to be especially effective in tackling this numerical problem. I developed an adaptive, see [**23**, **24**] Markov chain Monte Carlo Metropolis-Hastings algorithm to explore the parameter space Λ efficiently while requiring the least amount of tuning for the specific signal analysed; the code is an extension of the one developed by some collaborators to explore Markov chain Monte Carlo methods for binaries without spin [**9**, **10**] or one spin [**16**].

In the Markov chain Monte Carlo algorithm, a Markov chain crawl around the parameter space according to a specific set of rules:

- At iteration n, the chain is in the state $\vec{\lambda_n}$. Choose a proposal state $\vec{\lambda_k}$ with probability q_{nk}.
- Compute the acceptance probability α:

$$\alpha = min\left\{1, \frac{p(\vec{\lambda_k}\,|\vec{x}, M) q_{kn}}{p(\vec{\lambda_n}|\vec{x}, M)\, q_{nk}}\right\} \tag{1.40}$$

- Accept $\vec{\lambda_k} = \vec{\lambda_{n+1}}$ as the new state of the chain with probability α, otherwise $\vec{\lambda_n + 1} = \vec{\lambda_n}$ (with probability $1 - \alpha$)

The set of states $\vec{\lambda_n}$ of the chain following this procedure converges towards the posterior distribution.

I implemented parallel tempering [**25**, **26**, **27**] to improve the sampling. It consists of running several Markov chains in parallel, each with a different "temperature", which can swap parameters under certain conditions. The likelihood Eq. 1.34 is then modified to become:

$$\mathcal{L}_T \equiv p_T(\vec{x}|\vec{\lambda}, M) = p(\vec{x}|\vec{\lambda}, M)^{1/T} \tag{1.41}$$

Which has the effect to reduce the contrast of the likelihood surface and allow for an easier transition between modes. Only the $T = 1$ chain is used for estimating the posterior.

In Eq. 1.39 we applied Bayes' theorem to obtain the probability of a specific parameter vector value ($\vec{\lambda}$) given the observed data $\vec{x}$ and the model M. The theorem can also be applied to compute the probability of a specific *model* M_i given the observed data:

$$p(M_i|\vec{x}) = \frac{p(M_i)\,p(\vec{x}|M_i)}{p(\vec{x})}. \tag{1.42}$$

We compare the two models M_i and M_j by computing the *odds ratio*:

$$O_{i,j} = \frac{p(M_i|\vec{x})}{p(M_j|\vec{x})} = \frac{p(M_i)\,p(\vec{x}|M_i)}{p(M_j)\,p(\vec{x}|M_j)} = \frac{p(M_i)}{p(M_j)} B_{i,j}, \tag{1.43}$$

where

$$B_{i,j} = \frac{p(\vec{x}|M_i)}{p(\vec{x}|M_j)} \tag{1.44}$$

is the *Bayes factor* of the two models, and we recognise the evidence $p(\vec{x}|M_i)$ from Eq. 1.39. The evidence must be marginalised over the parameters of the model in order to compute the Bayes factor:

$$p(\vec{x}|M_i) = \int_\Lambda p(\vec{\lambda}|M_i)\,p(\vec{x}|\vec{\lambda}, M_i)\,\mathrm{d}\vec{\lambda}. \tag{1.45}$$

There are existing algorithms dedicated to the computation of this integral, and of the Bayes factor. For instance, *nested sampling* [**28**] has been shown to be very efficient in the case of non-spinning gravitational-wave sources [**13**], and can in addition be used to produce probability-density functions of the parameters. The odds ratio Eq. 1.43 is the quantity to look at to distinguish between two models. However it is difficult to estimate prior probabilities of models, unlike prior probabilities of parameters within a model, which often have clear astrophysical justifications (uniform in the sky for instance). Because of this I will quote Bayes factors (see Section 7.2) when trying to answer the question whether I can distinguish between models M_i and M_j, keeping in mind the possible prior factor $p(M_i)/p(M_j)$. As a by-product of the exploration of the parameter space with Markov chain Monte Carlo, it is possible to compute the evidences of the models used. For instance, the harmonic-mean method [29], in which the evidence is approximated by:

$$p(\vec{x}|M_i) \approx \sum_{k=1}^{N} p(\vec{\lambda}_k|M_i)\, p(\vec{x}|\vec{\lambda}_k, M_i)\, V_{\vec{\lambda}_k}, \tag{1.46}$$

where $\{\vec{\lambda}_k : k = 1, \ldots, N\}$ is the set of N points sampled by the Markov chain Monte Carlo, and $V_{\vec{\lambda}_k}$ is the volume of parameter space associated with the point $\vec{\lambda}_k$. Since the Markov chain Monte Carlo algorithm samples according to the posterior (and, up to a proportionality constant, converges towards posterior probability-density function), the density of points in the chain at a certain location $\vec{\lambda}_k$ in the parameter space Λ will become proportional to the posterior for large N. It follows that

$$\lim_{N\to\infty} V_{\vec{\lambda}_k} = \frac{\alpha_i}{p(\vec{\lambda}_k|M_i)\, p(\vec{x}|\vec{\lambda}_k, M_i)}, \tag{1.47}$$

with α_i a proportionality constant. We then have $p(\vec{x}|M_i) \approx \sum_{k=1}^{N} \alpha_i = N\,\alpha_i$, and obtain the estimate for α_i by considering the whole parameter space volume V_t:

$$V_t \approx \sum_{k=1}^{N} V_{\vec{\lambda}_k} = \sum_{k=1}^{N} \frac{\alpha_i}{p(\vec{\lambda}_k|M_i)\, p(\vec{x}|\vec{\lambda}_k, M_i)}. \tag{1.48}$$

Finally,

$$p(\vec{x}|M_i) \approx N\, V_t \left[\sum_{k=1}^{N} \frac{1}{p(\vec{\lambda}_k|M_i)\, p(\vec{x}|\vec{\lambda}_k, M_i)} \right]^{-1}, \tag{1.49}$$

which is the harmonic mean of the posterior values sampled by the Markov chain Monte Carlo. The issue with this method is that it gives too much weight to low-posterior points, which lie in a part of the parameter space that is badly sampled, by design, by the Markov chain Monte Carlo. The estimate of the evidence is then very sensitive to the quality of the sampling of a particular run. Another approach used in this work and referred to as *direct integration* [30] is to bin the samples obtained by the Markov chain Monte Carlo using a k-d tree and compute the integral by summing the contribution from each box. Lastly, I also use a well sampled subset of points [31] to estimate the probability constant α_i.

Throughout I will quote evidence relative to the Gaussian noise model, $\ln(Z) = \ln(p(\vec{x}|M_i)) - \ln(p(\vec{x}|M_{\text{Gaussian}}))$. The parameter spaces can be completely unrelated, even of different dimensionality, which allows for the comparison of models (which range from 9 parameters in the case of non-spinning systems, up to 15 in the case of a system with two spinning components).

1.3. Structure and Contribution of the Dissertation

I did the work presented in this dissertation as a member of the LIGO-Virgo Collaboration. It is an international effort to detect gravitational waves with ground-based observatories composed of ∼1380 members and ∼87 institutions. LIGO operates the detectors in the Hanford and Livingston sites in Washington state and Louisiana state, respectively. Virgo operates the detector in the Pisa site in Italy. My work took place in the Data Analysis part of the collaboration, in the Compact Binary Coalescence group, which focuses on the sources of the same name. Within this group I contributed mainly to the Parameter Estimation subgroup, whose goal is to extract astrophysical information from triggers that detection pipelines will provide. The ground-based detector network is entering its “Advanced” phase with Advanced LIGO and Advanced Virgo which will deliver an ten-fold improvement on the network sensitivity over initial LIGO-Virgo, and an increase by a factor of a thousand in the expect detection rate, see table 1.1, from [7].

The work presented in this dissertation consists on the development of methods and algorithms able to estimate all parameters of circularised binaries, showing that the exclusion of spin effects in the analysis leads to systematic biases greater than the typical statistical uncertainty, and use the code to conduct studies on spinning parameter estimation described in the following chapters.

1.4. Outline of the Chapters

Chapter 2 presents the results of the parameter estimation and model selection method applied to data from LIGO’s sixth science run and Virgo’s VSR2-3 science runs (July 07, 2009 to October 20, 2010). Even though no gravitational wave was detected, I illustrate my method on hardware and software injections.

Chapter 3 discusses degeneracies in sky localisation for gravitational waves. In particular, I investigate the two-detector network case and the influence of spin in the sky location recovery.

Chapter 4 presents some investigations on the effect of the inspiral-only waveform model on gravitational waveforms including the later merger and ring-down. The biases from using incomplete models are discussed.

Chapter 5 presents the use of the Bayesian inference methods to assess the effect real, non-Gaussian and non-stationary noise can have on parameter estimation under the usual Gaussian noise assumption in the construction of the likelihood.

Chapter 6 presents the development of a physically motivated jump proposal to explore the extrinsic parameter space. I compute analytical formula to predict the extrinsic parameters of the two modes present in a non-spinning, three-detector analysis.

Chapter 7 is an exploration of the discriminating power of the Bayes factor between the spinning and non-spinning models.

Chapter 8 presents my contribution to several collaborative projects for which I helped apply the method I developed.

CHAPTER 2

Parameter estimation for compact binary coalescence events with first-generation ground-based gravitational-wave interferometers

In this chapter, I describe the application of tools that I developed for LIGO-Virgo parameter estimation as part of the parameter-estimation sub-group of the LIGO-Virgo Collaboration to several simulated signals in the most recent detector data. I demonstrate that I can successfully recover the known parameters of these signals, subject to statistical measurement uncertainties and systematic biases due to differences between injected waveforms and the waveform families used for analysis.

2.1. Introduction

Binary systems of compact objects like black holes or neutron stars lose energy through the emission of gravitational radiation, as predicted by general relativity and confirmed through binary-pulsar observations [**2**, **32**]. During this process they emit a characteristic "chirping" gravitational wave signal of predominantly increasing amplitude and frequency that enters the observational band of the present generation of ground-based laser-interferometer detectors at $\lesssim 30$ Hz, sweeping through the detection band for a few seconds (depending on the masses of the objects) until they coalesce.

The search for gravitational wave signatures of compact-binary coalescence in LIGO's most recent sixth science run and Virgo's science runs 2 & 3 is described in [33]. Here, I describe the status of the next stage after the detection searches: parameter estimation and model selection.

Being able to accurately estimate the parameters of the merging binary, including the masses of the components, their spins, and the location of the binary on the sky, is a critical ingredient for enabling gravitational-wave astrophysics. Localizing the merger on the sky is crucial for a successful electromagnetic follow-up of the gravitational-wave detection, which is one of the possible approaches to multimessenger astronomy (see, e.g., [34, 35]). Obtaining information about compact masses and spins could lead to unexpected discoveries for individual events (for example, finding compact objects inside the surmised mass gap between neutron stars and black holes [36, 37]). Eventually, when multiple detections are available for analysis, inference about the distribution of the population of coalescing compact binaries will allow us to probe the astrophysics of binary evolution and dynamics of dense stellar environments (e.g., [38, 39]).

In Section 2.2 I give a brief overview of the analysis method. While no detections were claimed in [33], I illustrate this analysis using 4 Hardware and Software injection examples described in section 2.3. One of these hardware injections was performed without the knowledge of the data analysis teams as part of the “blind injection challenge”; it was successfully detected as reported in [33]. I conclude with the possible implications for gravitational-wave astronomy in section 2.4.

2.2. Analysis

Each data segment containing an injected signal was analysed using a Bayesian parameter-estimation method, which calculates the joint posterior probability density functions of the parameters of each model. The parameters form a parameter space for the model M, and a point in this space is denoted $\vec{\lambda}$. Parameters for the signal model include the component masses and spins (for some models), luminosity distance, location and orientation of the source.

The posterior probability-density function is generated from a prior distribution function $p(\vec{\lambda}|M)$, describing knowledge about the parameters within a model M before the data is analysed, and a likelihood function $p(\vec{x}|\vec{\lambda}, M)$, denoting the probability under model M of obtaining the dataset $\vec{x}$ for a given parameter set $\vec{\lambda}$. The model for the likelihood function, described in Section 1.2.4, is based on the assumption that the noise is stationary and Gaussian. Although it is not expected for this assumption to be precisely true for real detector noise, limited investigations suggest that this is an acceptable approximation when the data is of good quality, see Section 5.3, [40].

The high dimensionality of the parameter space, and the complicated structure of the likelihood function make it impractical to exhaustively calculate posterior quantities. Instead I rely on stochastic sampling of the posterior probability-density function, which then allows samples to be binned to produce histograms, which show the distributions. The analysis is performed using the *LALInference* platform of the LSC Algorithm Library [41], which allows calculation of the prior, likelihood and templates using standardised functions. Ensuring accurate sampling of the posterior probability-density function is a difficult task. The primary challenge of parameter estimation in a multi-dimensional parameter space lies in the difficulty of exploring a multi-modal posterior distribution with partially degenerate parameters. I applied several convergence diagnostics to ensure that the algorithm was indeed properly recovering the posterior distributions. I used 5 independent Markov chains to confirm convergence, and computed their Gelman-Rubin statistics [**42**] and autocorrelation functions. I checked that all chains reached the same maximum relative log likelihood, within the expected (number-of-parameters)/2 spread (4.5 in a non-spinning analysis, 7.5 with precessing spins). This estimate comes from the approximation of the likelihood surface to be Gaussian in the high signal-to-noise ratio limit. I also computed the evidence from Markov chain Monte Carlo results using direct integration [**30**].

I used a prior density functions uniform in the component masses with the range $1 \leq m_{1,2} \leq 30\,\mathrm{M}_{\odot}$, and with the total mass constrained by $m_1 + m_2 \leq 35\,\mathrm{M}_{\odot}$. The prior density function on the location of the source was taken to be uniform in volume, constrained between luminosity distances $d_L \in [1, 100]$ Mpc. I used an isotropic prior on the orientation of the orbital plane of the binary. I define the inclination, ι, to be the angle between the orbital angular momentum and the line of sight. For analyses using waveform models that account for possible spins, the prior on the spin magnitudes, a_1, a_2, was taken to be uniform in the range $[0, 1]$, and the spin angular momentum vectors were taken to be isotropic. The computational cost of the parameter-estimation pipeline precludes from running it on all times; therefore, the parameter-estimation search relies on an estimate of the coalescence time as provided by the detection pipeline [**33**]. In practice, a 200 ms window around this trigger time is sufficient to guard against the uncertainty in the coalescence time estimates from the detection pipeline, see for instance

Table 2.1. List of the waveform models used for the analysis. In all models, the inspiral phase of the binary evolution is described by the post-Newtonian (pN) expansion to 3.5pN order (2.5pN for spin effects when included) in phase, and Newtonian order (0pN) in amplitude, unless otherwise specified.

Model	Name	Spin effects	Ref.
TF2	TaylorF2	no	[44]
TF2_2	TaylorF2 @ 2pN	no	[44]
TF2_25 [1]	TaylorF2 @ 2.5 pN	no	[44]
ST_NS	STPN_noSpin	no	[45]
ST_SA	STPN_spinAligned	aligned	[45]
ST	STPN	yes	[45]
ST_25 [1]	STPN @ 2.5pN	yes	[45]

[1] Used only for the blind hardware injection

[43]. The results are not significantly affected by other astrophysically sensible choices of priors. I present the results using the chirp mass, $\mathcal{M} = (m_1 m_2)^{3/5}(m_1 + m_2)^{-1/5}$, and eta, $\eta = (m_1 m_2)/(m_1 + m_2)^2$, mass combinations.

I used seven different waveform models in this analysis. In all models, the inspiral phase of the binary evolution is described by the post-Newtonian (pN) (see Section 1.2.2) expansion to 3.5pN order (2.5pN for spin effects when included) in phase, and Newtonian order (0pN) in amplitude, unless otherwise specified. The models terminate at the end of the inspiral using a model-dependent condition to approximate the breakdown of the post-Newtonian expansion. Table 2.1 lists the approximants used. “Aligned” refers to both spin vectors being aligned to the orbital angular momentum of the binary. “STPN” refers to the SpinTaylor post-Newtonian waveform for precessing binaries in LAL [41].

In the case of the blind injection analysis discussed in section 2.3.3, templates with the inspiral phase computed up to 2.5pN order where also used, as the injected waveform included terms only up to 2.5pN.

Data from the multi-detector network consisting of two LIGO instruments (H1 and L1) and Virgo (V1) were used coherently in the analysis. The sampling rate was 2048 Hz, corresponding to a 1024 Hz Nyquist frequency, high enough to include the entire waveform for all models, except in the case of waveforms including post-inspiral stages, which have a negligible contribution to the signal-to-noise ratio at higher frequencies. The 32 second segments of time-domain data were Tukey windowed, with a 0.4 s roll-off on either side of the segment. The power spectral density (PSD) of the instrumental noise was estimated using 1024 s of data after the end of the analyzed segment. I verified that varying the methods of power-spectral-density estimation (using ±512 seconds spanning the signal trigger time, and using median and mean estimation methods), had a negligible effect on the parameter-estimation results, smaller than the systematic uncertainties of parameter estimation.

Calibration errors, which can influence the reconstructed amplitude, phase, and timing of the data [46], have the potential to affect parameter-estimation results. An analysis of the effect of calibration errors, which considered mock errors similar to those expected during the S6 and VSR2/3 runs, concluded that such errors are unlikely to cause a significant deterioration in parameter-estimation accuracy [47].

2.3. Simulations

Over the course of the LIGO S6 and Virgo VSR2/3 science runs a series of hardware injections have been carried out where the arm lengths of the three detectors were physically changed to simulate the passing of a gravitational wave.

Table 2.2. Parameters of hardware (HW) and software (SW) injected signals. Non-spinning injections were generated using the EOBNR waveform model, whereas spinning injections used the SpinTaylor model. The SNR column shows optimal network signal-to-noise ratio.

§	HW/SW	$\mathcal{M}$	m_1	m_2	d_L	ι	$\lvert a_1\rvert$	$\lvert a_2\rvert$	SNR
2.3.1.1	HW	3.865	4.91	4.02	36.2	0.46	0	0	13
2.3.1.2	SW	3.865	4.91	4.02	36.2	0.46	0	0	13
2.3.2.1	SW	4.76	6	5	30.0	0.02	0.6	0.8	19
2.3.3	HW	4.96	24.81	1.74	24.37	1.91	0.57	0.16	16

Table 2.3. Logarithm of the evidence $\ln(Z)$ for each injection and each waveform family obtained via direct integration. The numbers come with error bars of ±5.

§	TF2	TF2_2	TF2_25	ST_NS	ST_SA	ST	ST_25
2.3.1.1	66	68	-	67	70	68	-
2.3.2.1	155	151	-	158	160	163	-
2.3.3	-	-	130	-	-	-	211

As an end-to-end test of the search pipeline during the science runs, a signal was added to the data via a hardware injection, with parameters that were unknown ("blind") to the data analysts. The parameters and template family were revealed only after the search was complete, and I include a retrospective analysis of this blind injection in section 2.3.3 (see [48] for parameter estimation carried out before the injection was revealed).

I have also made several simulated software injections into real detector noise from those runs. Below, I describe the results of parameter-estimation analysis of several of these injections, whose injection parameters are listed in Table 2.2.

I present the posterior probability density functions on the source parameters using a coherent, multi-detector data model with the seven waveform families described above.

2.3.1. Non-spinning hardware injections

2.3.1.1. Binary black hole. I first describe the analysis of a hardware injection corresponding to a non-spinning black-hole binary with $4.91M_\odot$ and $4.02M_\odot$ components, injected at a network signal-to-noise ratio of 13. This injection was made with effective-one-body – numerical-relativity (EOBNR) waveforms, using the *EOBNRv1* version [49].

Figure 2.1 shows a comparison of the posterior probability-density function of the mass parameters for different models. The chirp mass has a low statistical uncertainty of $\sim 1\%$, with the greatest statistical uncertainty claimed by models that allow for non-zero spin magnitudes due to inter-parameter degeneracies. The 90% confidence intervals on the chirp mass obtained with TaylorF2 templates just exclude the true value, an indication of the systematic bias due to the systematic waveform differences between the injected EOBNR waveform and these templates. These differences are also responsible for the particularly strong bias in the symmetric mass ratio η for 2.0pN TaylorF2 templates, exceeding the statistical measurement uncertainty in this parameter. In contrast, I find that by using the 3.5pN TaylorF2 templates the systematic bias is reduced to less than the statistical error. The uncertainty in the mass ratio is typically larger than that in the chirp mass, leading to the characteristic thin, correlated joint distribution for m_1 and m_2, referred to as a “banana shape”.

Figure 2.2 shows the most relevant extrinsic parameters of the binary black hole source: the recovered sky position, distance and inclination angle. The correlations between intrinsic parameters (masses and spins) and extrinsic parameters are generally weaker than correlations between different parameters within the same group. Thus, models that include or exclude spins have similar statistical measurement uncertainties for extrinsic parameters.

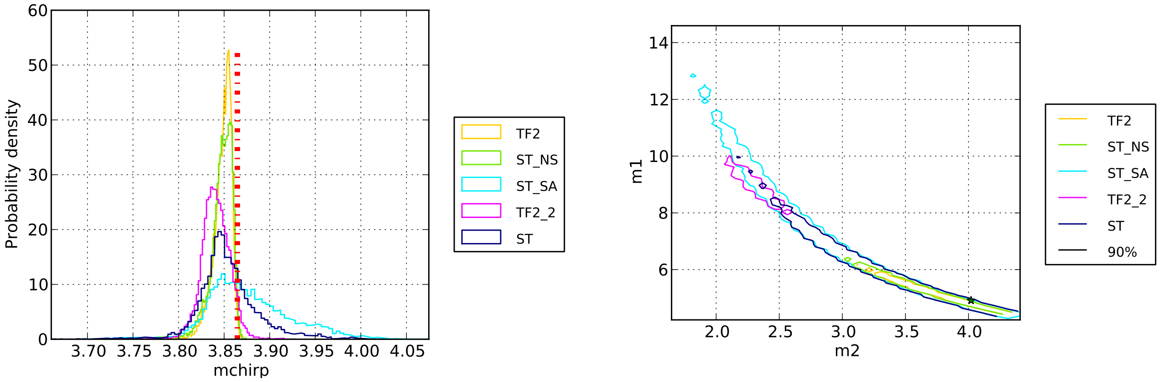

Figure 2.1. (left) Posterior probability distributions for the chirp mass $\mathcal{M}$ of the non-spinning binary black hole hardware injection (section 2.3.1.1) for all signal models. The injected value is marked with a vertical red line. (right) Overlay of 90% probability intervals for the joint posterior distribution on the component masses m_1, m_2 of the binary. The true value is marked by the green star. Models which allow for non-zero spins find wider probability-density functions for the coupled mass parameters. The true value is marked with a green star.

Finally, figure 2.3 shows individual posteriors for the two dimensionless spin magnitudes, obtained using the model ST (table 2.1), full-spin STPN waveforms. Although spin is not very strongly constrained, particularly for the lower-mass secondary, both spin measurements are consistent with the true value of 0 spin. The absence of strong constraint is due to a combination of the low mass ratio m_1/m_2 and nearly face-on inclination, see section 2.4 for details. This inability to constrain the spin is reflected in the evidence for each template family, shown in table 2.3, where all models have the same evidence within the error bars.

2.3.1.2. Comparison with software injections. To compare between results from hardware injections and software injections, I replicated the non-spinning binary black hole hardware injection (section 2.3.1.1) in software at three different times. Figure 2.4

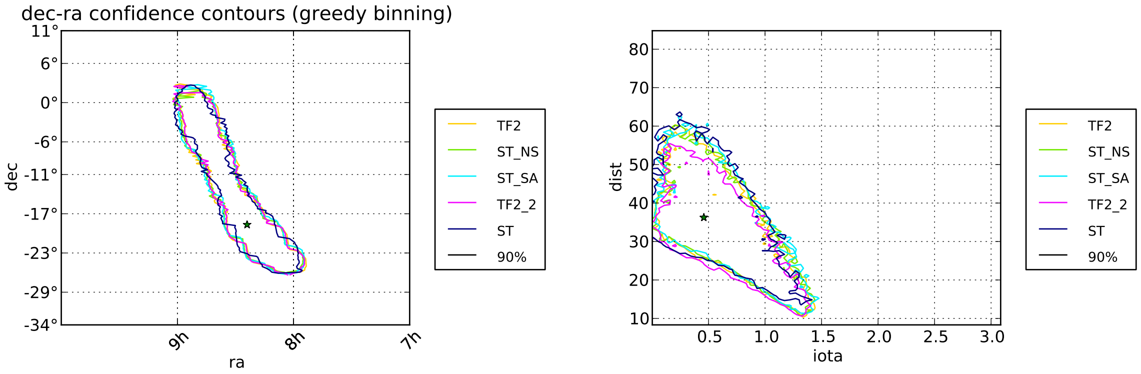

Figure 2.2. Joint posterior probability distributions for the location and inclination angle of the non-spinning binary black hole hardware injection (section 2.3.1.1). (left) The binary can be constrained to two contiguous regions of the sky representing the reflection of the source location through the plane of the detectors. (right) The distance and inclination, like the sky location, are estimated with a similar accuracy in models that include or exclude spins.

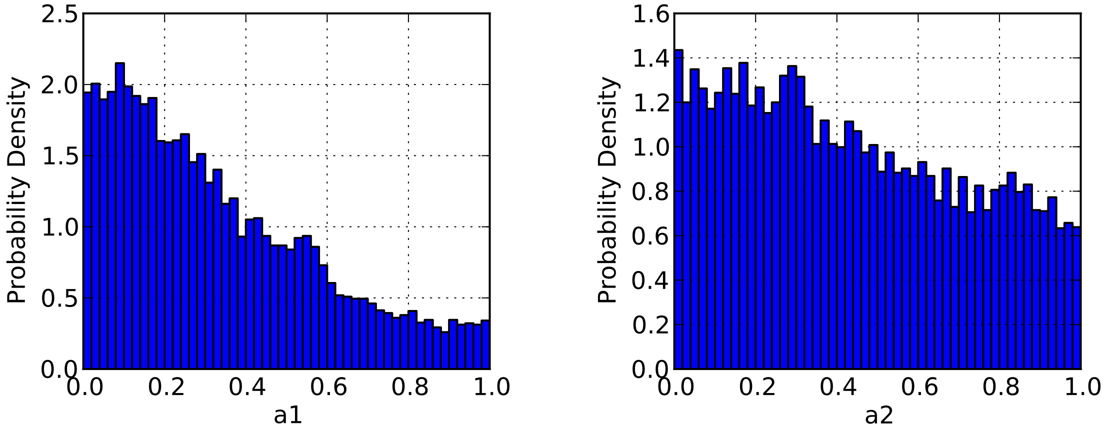

Figure 2.3. Posterior probability distributions for the dimensionless spin magnitude of the heavier (left) and lighter (right) components of the binary from the non-spinning binary black hole hardware injection (section 2.3.1.1), as inferred in the model ST (table 2.1), full-spin STPN.

shows the recovered probability-density functions for the chirp mass and the joint inclination and distance distribution for the hardware injection, and identical software injections

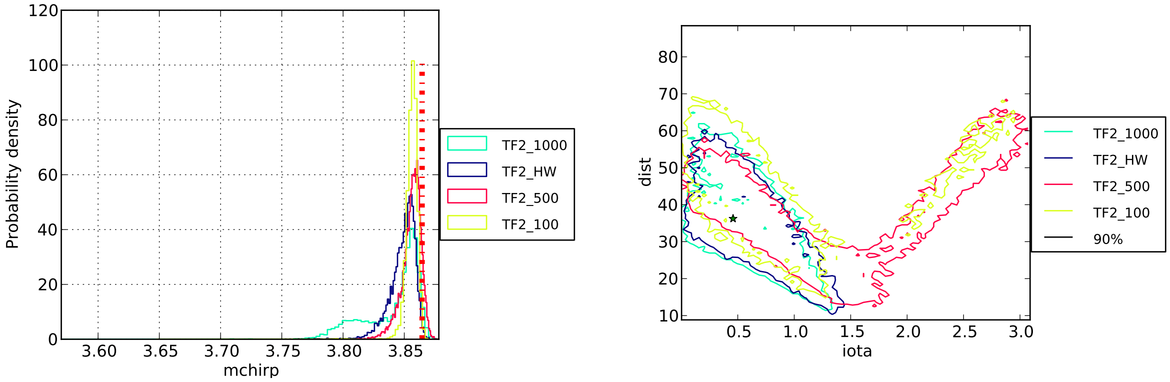

Figure 2.4. (left) Posterior probability distributions for the chirp mass $\mathcal{M}$ of the non-spinning binary black hole injection for signal model TF2 (table 2.1), TaylorF2 at 3.5 pN order, for the hardware injection (section 2.3.1.1) and 3 software injections of the same parameters injected 100, 500 and 1000 seconds before the hardware injection (1a_100, 1a_500 and 1a_1000 respectively, section 2.3.1.2). The injected value is marked with a vertical red line. (right) Overlay of 90% probability intervals for the joint posterior distribution on the inclination and distance of the binary. Different realisations of the noise, rather than differences between hardware and software injections, are the likely reason for the variations in recovered probability-density functions.

100, 500 and 1000 seconds before the hardware injection. There are some variations in the recovered parameter probability-density functions, but the hardware injection is not an outlier. Rather, these variations are likely due to differences in the realisation of the noise between the segments being analysed. It appears that this effect dominates any systematic error introduced by the method of performing the hardware injection, such as the actuation function used in modelling the impulse applied to the mirrors to produce the desired signal.

2.3.2. Spinning software injections

2.3.2.1. Binary black hole. I simulated the signal from a binary black hole with misaligned spinning components with a SpinTaylor software injection. This binary consists of $6M_\odot$ and $5M_\odot$ black holes, with dimensionless spin magnitudes of 0.6 and 0.8, respectively, and an optimal network signal-to-noise ratio of 19. The misalignment between the spins and the orbital angular momentum cause the plane of the binary to precess, producing modulations in the received gravitational-wave signal.

Figure 2.5 shows a comparison of the posterior probability-density functions of the mass parameters inferred with different signal models. The mass ratio is again severely biased for the 2pN TaylorF2 model, which is not surprising for a 3.5pN injection with spinning components as both the post-Newtonian order and the spin alter the phase evolution of the signal.

Figure 2.6 shows the recovered sky location, distance and inclination angle of the source. The conclusions are quantitatively similar to those in section 2.3.1.1. The joint distance-inclination posterior displays a characteristic “V-shape” degeneracy, which prevents either parameter from being measured accurately.

The spin magnitudes are again poorly constrained, with non-zero support across the entire allowed range, as shown in figure 2.7. Even though the injected signal was simulated from a system with high spin magnitudes (0.6 and 0.8), the low mass ratio m_1/m_2, the near anti-alignment of the spins with the orbital angular momentum and the face-on inclination conspire to give the poor spin estimates, see section 2.4 for details. In addition, with this weak precession effect, the spin tilts (angles between the spin vector and the orbital angular momentum) are also poorly constrained. A comparison of the evidences

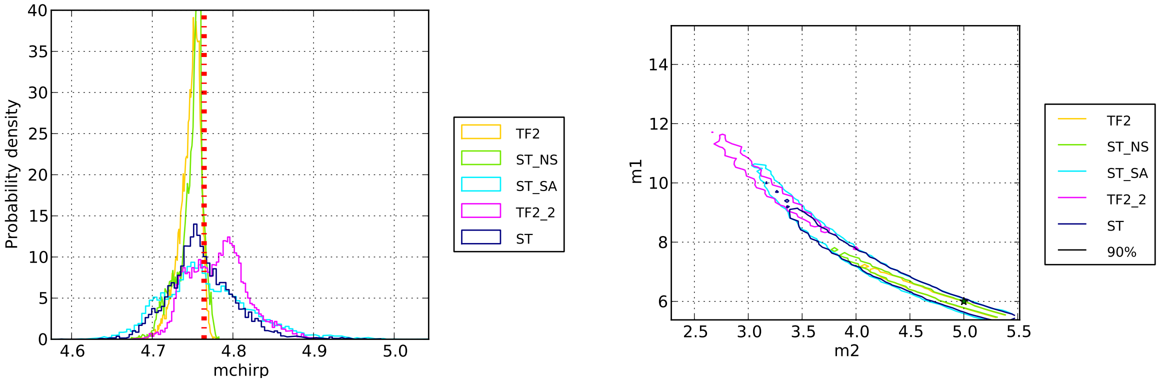

Figure 2.5. (left) Posterior probability distributions for the chirp mass $\mathcal{M}$ of the spinning binary black hole software injection (section 2.3.2.1) for all signal models. The injected value is marked with a vertical red line. (right) Overlay of 90% probability intervals for the joint posterior distribution on the component masses m_1, m_2 of the binary.

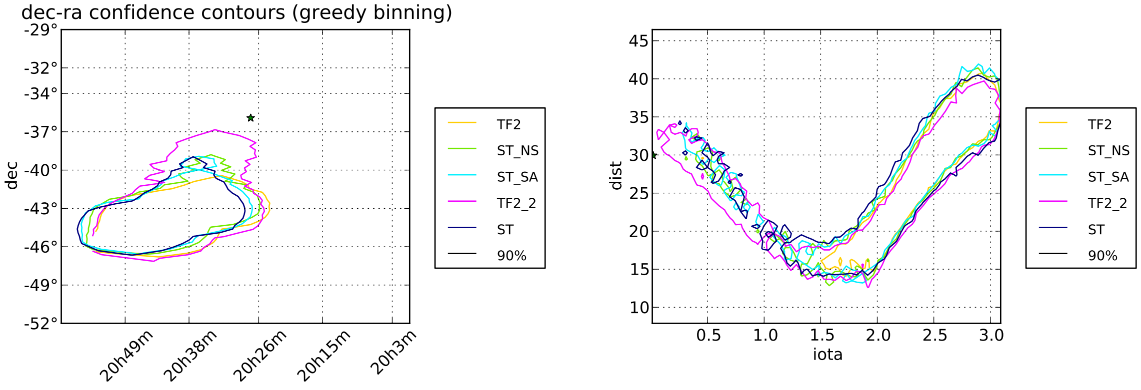

Figure 2.6. Joint posterior probability distributions for the location and inclination angle of the spinning binary black hole software injection (section 2.3.2.1). (left) The binary is localized well on the sky. (right) The characteristic "V-shape" degeneracy in distance and inclination prevents either parameter from being accurately constrained individually.

in table 2.3 indicated that all models have the same evidence within the error bars, with a slight increase for spinning models.

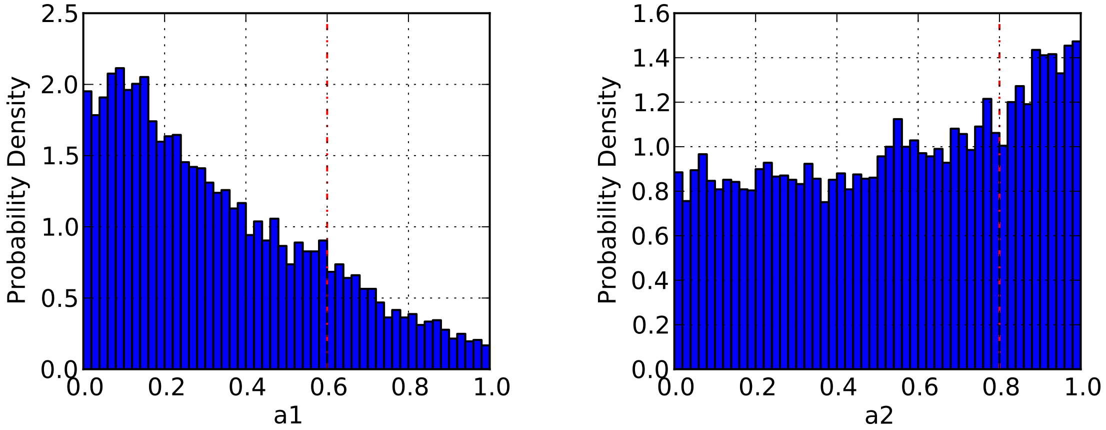

Figure 2.7. Posterior probability distributions for the dimensionless spin magnitude of the heavier (left) and lighter (right) components of the binary from the spinning binary black hole software injection (section 2.3.2.1), as inferred in the model ST (table 2.1), full-spin STPN; the true values are shown with vertical red lines.

2.3.3. Blind hardware injection

The search pipeline described in [33] identified a gravitational-wave candidate occurring on 16 September 2010 at 06:42:23 UTC. A Bayesian analysis was performed using the algorithms and implementations described above, where parameter estimates varied significantly depending on the exact model used for the gravitational waveform.

Following the completion of the analysis, the event was revealed to be a blind injection. Further investigation revealed several problems:

- The template signal included phase corrections only up to 2.5pN order, which is an outlier in the post-Newtonian expansion, see [50]. Parameter estimation was not carried out with templates at this order, leading to a significant bias in the mass ratio, and hence the component masses.

- The signal to be injected in the Hanford and Livingston sites had the wrong sign, causing strong biases in the extrinsic parameters.
- Lastly, a software bug artificially set to zero one of the terms in the injected waveform.

I present here an analysis using templates at 2.5pN order in phase. I artificially introduce a sign flip in the templates for Hanford and Livingston detectors in order to match the injected waveform. Figure 2.8 shows a comparison of the posterior probability-density functions of the mass parameters for TaylorF2 and SpinTaylor waveform models. The fully spinning, precessing analysis with SpinTaylor templates at 2.5pN order in phase (i.e., the same template as used in the injection, up to the injection software bug) centres on the correct masses for this neutron-star – black-hole system, $24.81M_{\odot}$ and $1.74M_{\odot}$. However, the systematic error due to fixing spin to zero in the analysis of this spinning injection is significant, and leads to the wrong conclusion that a binary black hole system is observed if the TaylorF2 model is used.

Figure 2.9 shows the recovered sky position, distance and inclination angle of the source. The sky location recovered is contained in several distinct regions, spread in a half circle on the sky. This behaviour is consistent with two detectors contributing the majority of the signal-to-noise for this source. On top of this first-order constraint, spin projection effects can break the degeneracy, as discussed in Section 3.4, [8].

The large mass ratio, $m_1/m_2 = 25 : 1.7$, and the high inclination allows for the magnitude of the spin of the massive component to be measured with an accuracy $\lesssim 10\%$. Meanwhile, the spin of the light component is unconstrained, and the posterior on its

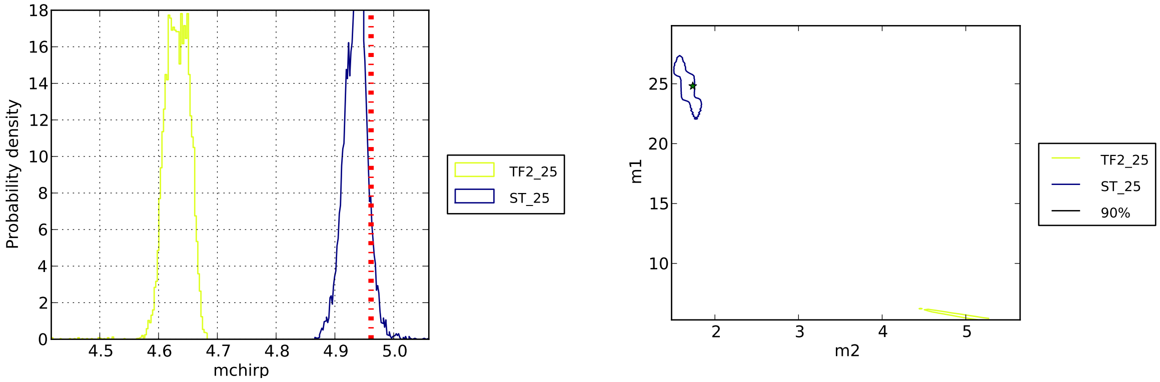

Figure 2.8. (left) Posterior probability distributions for the chirp mass $\mathcal{M}$ of the blind injection (section 2.3.3) for all signal models. The injected value is marked with a vertical line. (right) Overlay of 90% probability intervals for the joint posterior distribution on the component masses m_1, m_2 of the binary. The bias introduced by an analysis with a model which disallows spin is clear.

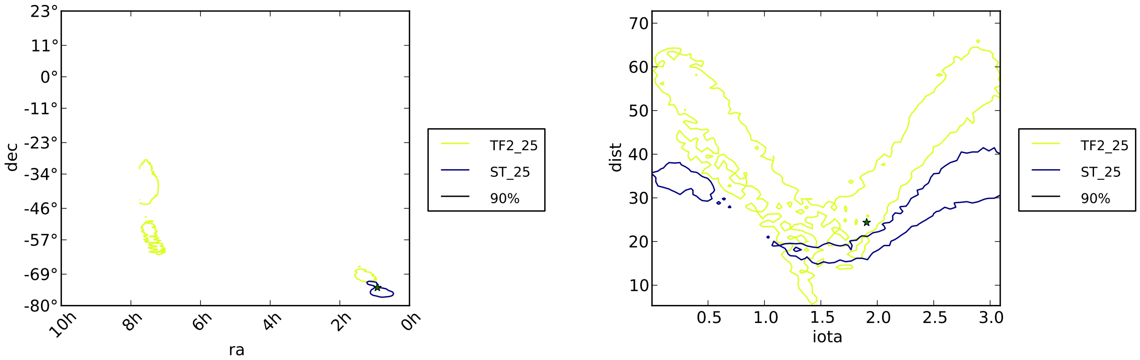

Figure 2.9. Joint posterior probability distributions for the location and inclination angle of the blind injection (section 2.3.3). (left) The sky location is constrained to several distinct regions lying along a half circle on the sky. (right) Again, the characteristic "V-shape" degeneracy in distance and inclination is evident.

magnitude is consistent with the prior. Correspondingly, the evidences in table 2.3 favour the spinning model. See section 2.4 for further explanations on spin measurements.

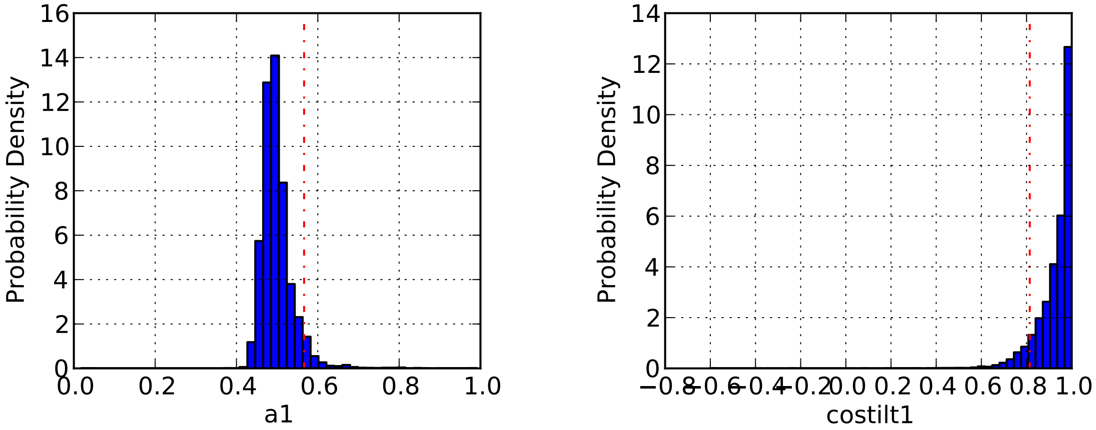

Figure 2.10. Posterior probability distributions for the dimensionless spin magnitude (left) and tilt angle (angle between the spin vector and the orbital angular momentum, measured at 40Hz, right) of the heavier component of the binary from the blind injection (section 2.3.3), as inferred with model ST (table 2.1), full-spin STPN; the true values are shown with vertical red lines. The large mass ratio m_1/m_2 allows for the spin of the massive component to be measured. On the other hand, the spin of the light component is unconstrained.

2.4. Implications for gravitational-wave astronomy

In this section, I have demonstrated the application of a suite of Bayesian parameter-estimation tools to hardware and software injections from the last initial LIGO and Virgo science runs. I have shown that those tools are able to explore complicated multi-dimensional parameter spaces, construct posterior probability distribution functions using a variety of waveform models, and compare these alternative models.

For some parameters, such as the distance to the source and the binary's sky location, the accuracy of inference is limited by the measurement uncertainty of an observation with finite signal-to-noise ratio, as well as by degeneracies between parameters. For example, the overall signal amplitude may be measured with good accuracy, but the amplitude is affected by several physical parameters (e.g., distance, inclination angle, . . .); so that while the observed data do place constraints on the parameter space, significant uncertainties remain in the estimates of individual parameters.

For other parameters, such as the chirp mass, which can be determined to an accuracy of $\lesssim$ few % within a given waveform model, the systematic errors (estimated as the differences between results for different waveform families) can dominate the statistical measurement uncertainties. Therefore, improvements in waveform accuracy, based on a combination of analytical and numerical work, will be crucial for accurate parameter reconstruction in the advanced detector era.

What properties are important in the source system in order to measure its spin parameters is a very complex question. The work in this chapter is only looking at a few examples while a complete answer requires a further systematic study currently underway, see Section 7. I can however make the following statements based on theoretical grounds and on the experiments described in this chapter as well as in other publications in preparation. A signal from a non-spinning binary has both polarisations nearly identical, regardless of inclination, while a signal from a spinning source has a greater difference between its polarisations as the inclination gets close to edge-on, due to the precession of the orbital plane. This key difference makes a spinning signal more distinguishable and its spin more measurable in an edge-on configuration, for the same signal-to-noise ratio. (To see if a plate is wobbling, one will want to see it from the side). In addition, a high mass ratio m_1/m_2 allows for the spin magnitude of the most massive component to be measured, while degrading the accuracy of the spin magnitude of the least massive component. Misalignment between the spins and the orbital angular momentum provide additional information to constrain spins, both the magnitudes and angles.

Although there has been rapid progress in the field of gravitational-wave parameter estimation, a number of key questions remain. Some of these are already being addressed, or will be addressed over the next few years before advanced detectors come online. An incomplete list includes:

- How precisely will we be able to measure spin magnitudes and spin tilt angles in precessing neutron star-black hole and binary black hole systems?
- How important are systematic waveform errors due to imperfect waveform knowledge for various system classes? What are the accuracy requirements on waveform families for parameter estimation?
- What is the best way to handle the long-duration signals in advanced detectors with their extended bandwidth?
- How accurately can we measure finite-size and tidal-dissipation effects for systems involving neutron stars?
- How is parameter estimation affected when the background noise is not stationary and Gaussian?

I anticipate that the analyses carried out here will be directly applicable to the first detections from the advanced detector era, allowing for astrophysical inference and measurement of masses, spins, and sky locations of coalescing compact binaries. This, in turn, will improve searches for electromagnetic counterparts, and ultimately allow to solve a key “inverse problem” of gravitational-wave astrophysics: to reconstruct binary evolution and dynamical binary formation from the observed distributions of masses and spins of merging compact binaries.

CHAPTER 3

Degeneracies in sky localisation determination from a spinning coalescing binary through gravitational-wave observations: a Markov chain Monte Carlo analysis for two detectors.

I present in this chapter a specific example of the power of parameter-estimation methods, considering source localisation in the sky and analysing the degeneracy in it when data from only two detectors are used. I focus on the effect that the black-hole spin has on the localisation estimation. I also report on a comparative Markov chain Monte Carlo analysis with two different waveform families, at 1.5 and 3.5 post-Newtonian order.

3.1. Introduction

The measurement of source properties holds major promise for improving our astrophysical understanding and requires reliable methods for parameter estimation. This is a challenging problem, however, because of the large number of parameters (9 for circular non-spinning binaries, and more for spinning systems) and the significant amount of structure in the parameter space. In the case of high mass-ratio binaries (*e.g.* black hole-neutron stars), these issues are amplified for significant spin magnitudes and large misalignments between the black-hole spin and the orbital angular momentum [**51**, **52**, **45**]. However, the presence of spins improves parameter estimation through the signal modulations, although still presenting a considerable computational challenge. This was highlighted in the context of LISA observations [53, 54] and in a first study using Markov chain Monte Carlo with spinning signals devoted to ground-based observations [55].

In this chapter I examine the potential for parameter estimation of spinning binary inspirals with ground-based interferometers. [9, 10] explored parameter estimation for non-spinning binaries, which requires 9 parameters. I focus here on black hole-neutron stars binaries, which can exhibit significant coupling between the orbital angular momentum and the black-hole spin, mainly because of the high mass-ratio [51], while at the same time I am justified to ignore the neutron-stars spin, leading to a 12-dimensional parameter space (and sky localisation is of special interest for binaries containing at least one neutron star because of possible electromagnetic counterpart). I apply the Markov chain Monte Carlo algorithm to spinning inspiral signals injected into synthetic noise and I derive posterior probability-density functions (PDFs) of all twelve signal parameters. In a previous study [55], the parameter-estimation group at Nothwestern University showed the accuracy obtained in sky-position determination using data from a two-detector network, where a degeneracy in the sky position exists, and from a three-detector network, where the degeneracy is broken. Following this work, I analyse in further detail the degeneracy which is present when data from only two detectors are used. In section 3.4.2 I show that the degeneracy in the sky position is reduced but not lifted when a significant spin is present ($a_{\mathrm{spin}} \geq 0.5$), and that a sufficient angle between spin and orbital angular momentum can break such a degeneracy ($\theta_{SL} \geq 55^{\circ}$). In this study, I demonstrate that these degeneracies are due to a high degree of similarity between signals from sources with significantly different parameter sets, while I made sure the observed effects are real and not in fact artefacts due to potential errors in the analysis methodology.

This study on extrinsic parameters was done with templates at 1.5 post-Newtonian order. In section 3.4.3, I also demonstrate that the inclusion of higher post-Newtonian orders in the waveform can improve the accuracy of intrinsic parameter estimation.

3.2. Signal and observables

In this chapter I analyse the signal produced during the inspiral phase of two compact objects of masses $M_{1,2}$ in circular orbit. I focus on a fiducial black hole-neutron star binary system with $M_1 = 10\,\mathrm{M}_\odot$ and $M_2 = 1.4\,\mathrm{M}_\odot$, and I ignore the neutron-star spin. The black-hole spin $\mathbf{S}$ couples to the orbital angular momentum $\mathbf{L}$, leading to amplitude and phase modulations of the observed gravitational radiation due to the precession of the orbital plane. Here I model gravitational waves by post-Newtonian (pN) waveforms, either at 1.5pN order in phase and Newtonian amplitude or at 3.5pN order in phase and Newtonian amplitude. For the latter waveform I use the implementation from the LSC Algorithm Library (LAL) [56]. In the analysis I model the noise in each detector as a zero-mean Gaussian, stationary random process, with one-sided noise spectral density $S_a(f)$, at the initial-LIGO design sensitivity [57].

3.2.1. Waveform template at the 1.5pN order

I adopt the *simple-precession* limit, Eqs. 51, 52, 59 & 63 in [51], appropriate for the single-spin system considered here. For simplicity (to speed up the waveform calculation), I also ignore the *Thomas precession* [51]. In this approximation, the orbital angular momentum $\mathbf{L}$ and spin $\mathbf{S}$ precess with the *same* angular frequency around a fixed direction $\hat{\mathbf{J}}_0 \approx \hat{\mathbf{J}}$, where $\mathbf{J} = \mathbf{L} + \mathbf{S}$. During the inspiral phase the spin misalignment $\theta_{SL} \equiv \arccos(\hat{\mathbf{S}} \cdot \hat{\mathbf{L}})$

and $S = |\mathbf{S}|$ are constant. These approximate waveforms retain (at the leading order) all the prominent qualitative features introduced by the spins, while allowing to rapidly compute the waveforms analytically. While this approach is justified for the exploration of gravitational-wave astronomy and the development of parameter-estimation algorithms, more accurate waveforms [**58**, **59**, **60**, **61**]*e.g.* will be necessary for the analysis of real signals (see section 3.4.3).

A circular binary inspiral with one spinning compact object is described by a 12-dimensional parameter vector $\vec{\lambda}$. With respect to a fixed geocentric coordinate system my choice of independent parameters is:

$$\vec{\lambda} = \{\mathcal{M}, \eta, \mathrm{R.A.}, \sin \mathrm{Dec}, \sin \theta_{J_0}, \phi_{J_0}, \log d_{\mathrm{L}}, a_{\mathrm{spin}}, \cos \theta_{SL}, \phi_{\mathrm{c}}, \alpha_{\mathrm{c}}, t_{\mathrm{c}}\}, \tag{3.1}$$

where $\mathcal{M} = \frac{(M_1 M_2)^{3/5}}{(M_1+M_2)^{1/5}}$ and $\eta = \frac{M_1 M_2}{(M_1+M_2)^2}$ are the chirp mass and symmetric mass ratio, respectively; R.A. (right ascension) and Dec (declination) identify the source position in the sky; the angles $\theta_{J_0} \in \left[-\frac{\pi}{2}, \frac{\pi}{2}\right]$ and $\phi_{J_0} \in [0, 2\pi[$ identify the unit vector $\hat{\mathbf{J}}_0$; d_{L} is the luminosity distance to the source and $0 \leq a_{\mathrm{spin}} \equiv S/M_1^2 \leq 1$ is the dimensionless spin magnitude; ϕ_{c} and α_{c} are integration constants that specify the gravitational-wave phase and the location of $\mathbf{S}$ on the precession cone, respectively, at the time of coalescence t_{c}, defined with respect to the centre of the Earth.

3.2.2. Waveform template in the 3.5pN order

Although the 1.5pN, simple-precession waveform is useful to investigate the principal effects of spin on parameter estimation, a more realistic waveform is needed to analyse detected signals. The waveform I use for this is 3.5-pN in phase and Newtonian amplitude.

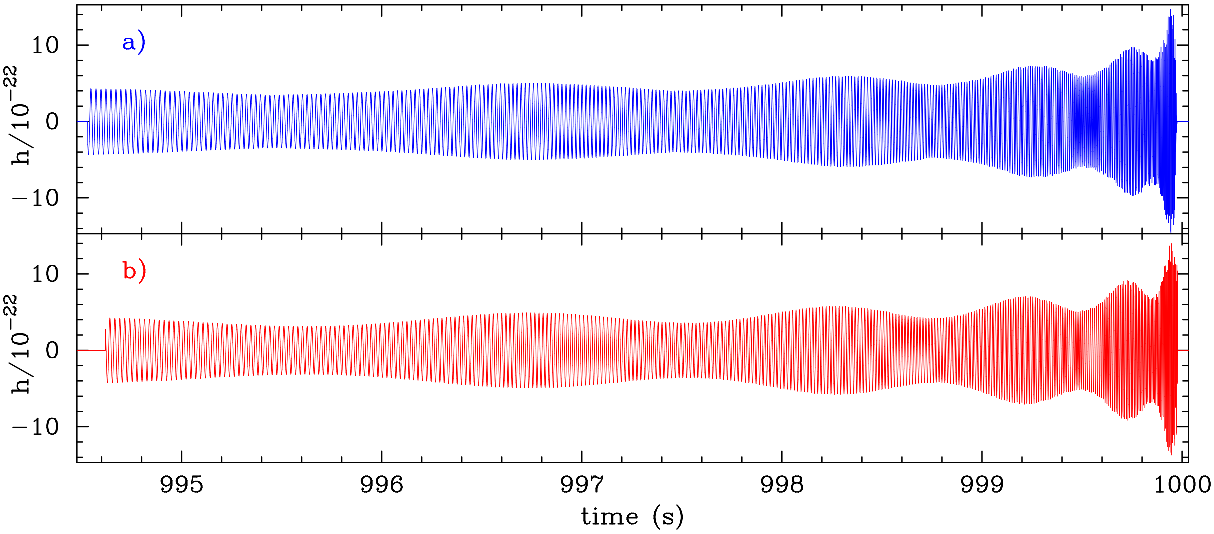

Figure 3.1. **(a)** Part of the 1.5pN time-domain waveform from a source with $a_{\text{spin}} = 0.5$ and $\theta_{SL} = 20°$. **(b)** The 3.5pN waveform from a source with the same parameters. The waveforms start at 40 Hz and are aligned at the coalescence time.

The implementation in the LSC Algorithm Library closely follows the first section of [45]. For comparison purposes I converted the usual set of parameters used in the LAL software to the parameters in Eq. 3.1. In doing so, I fix 3 of the 15 parameters of the LAL parameter set, setting the spin of the second member of the binary to be 0. The waveform is generated using `LALGenerateInspiral()` from the injection package [56]. An example of $h_a(t)$ for $a_{\text{spin}} = 0.5$ and $\theta_{SL} = 20°$ for both waveforms is shown in figure 3.1.

3.3. Parameter estimation: Methods

The goal of this analysis is to determine the *posterior* probability density function (PDF) of the unknown parameter vector $\vec{\lambda}$ in Eq. 3.1, given the data sets x_a collected by a network of n_{det} detectors and the *prior* $p(\vec{\lambda})$ on the parameters. I use wide, flat priors (see [16] for details). Bayes' theorem provides a rigorous mathematical rule to assign such a probability:

$$p(\vec{\lambda}|x_a) = \frac{p(\vec{\lambda})\,\mathcal{L}(x_a|\vec{\lambda})}{p(x_a)}\,; \tag{3.2}$$

The details and justifications on the application of this theorem are described in Section 1.2.4.

3.4. Parameter estimation: Results

3.4.1. Markov chain Monte Carlo runs

Here I present results obtained by injecting a signal into simulated interferometer noise and computing the posterior probability-density functions with Markov chain Monte Carlo techniques, for a fiducial source consisting of a $10\,M_\odot$ spinning black hole and a $1.4\,M_\odot$ non-spinning neutron star in a binary system at a distance of about 16 Mpc (see sections 3.4.2 and 3.4.3 for parameter values). I consider a number of cases for which I change the black-hole spin parameters. I run the analysis using the simulated data from (i) the 4-km LIGO detector at Hanford (H1) alone, (ii) the LIGO Hanford (H1) and a second detector with the initial-LIGO noise curve located and oriented in the same way as the Virgo detector near Pisa, which I denote by (P).

The Markov chain Monte Carlo analysis that I carry out on each data set consists of 5 to 25 independent chains, each with a length of several million iterations. The chains are sampled after a *burn-in* period see *e.g.* [**17**] that is determined automatically as follows: I determine the absolute maximum likelihood $\log(\mathcal{L}_{\max})$, defined as the highest likelihood $\log[\mathcal{L}(\vec{x}|\vec{\lambda})]$ obtained over the ensemble of parameters $\vec{\lambda}$ for which the overlap has been computed, for any of the individual chains. Then for each chain I include all the iterations *after* the chain reaches a likelihood value of $\log(\mathcal{L}_{\max})-2$ for the first time. All the Markov chains start at offset (*i.e.*, non-true) parameter values, unless specified otherwise. The starting values for $\mathcal{M}$ and $t_{\rm c}$ are drawn from a Gaussian distribution centred on the true parameter value, with a standard deviation of $0.1\,M_\odot$ and 30 ms respectively. The other ten parameters are drawn uniformly from the allowed ranges.

3.4.2. A Ring in the Sky

For the study in this section, I use the 1.5pN waveform with the *simple-precession* prescription only (see section 3.2.1). In order to further speed up the Markov chain Monte Carlo runs, I fixed the mass and spin parameters to the true parameter values, and performed test calculations to verify that this does not affect the conclusions.

As reference Markov chain Monte Carlo runs (experiment 1, see table 3.1), I injected signals into two simulated detectors (H1 and P). I made three different injections, which differed in the spin magnitude values ($a_{\rm spin} = 0.0, 0.5$) and the spin-misalignment values ($\theta_{SL} = 20^\circ, 55^\circ$) for $a_{\rm spin} = 0.5$ case; the remaining parameters were kept constant across all three injections: $\mathcal{M} = 3.0M_\odot$, $\eta = 0.11$ ($M_1 = 10.0M_\odot$, $M_2 = 1.4M_\odot$), $d_{\rm L} = 16\,$Mpc, R.A. $= 14.3\,$h, Dec $= 11.5^\circ$, $\theta_{J_0} = 3.8^\circ$, $\phi_{J_0} = 289^\circ$, $\phi_{\rm c} = 305^\circ$, $\alpha_{\rm c} = 4^\circ$ and $t_{\rm c} = 700009012.345\,$s GPS time.

For a detection with two interferometers, the sky position is degenerate; when no spin is present in the source, the probability-density functions show an incomplete sky ring where the source might be — long arcs separated by empty “gaps” — rather than one tightly constrained ring. When the black hole is spinning, and especially when the misalignment angle between orbital angular momentum and spin is significant, the sky

Table 3.1. List of the experiments described in section 3.4.2. The sky ring is defined as the ring produced by experiment 1, composed of arcs and gaps.

experiment	injection position (in the sky ring)	sky position parameters	starting values (in the sky ring)
1	arc	free	offset (non true values)
2a	arc	fixed	true position (arc)
2b	arc	fixed	gap position (◯)
3	gap (◯)	free	offset (non true values)

location constraint shrinks appreciably until much smaller arcs — or even a single arc — are left (see figure 3.2a).

In order to probe the nature of the gaps in the sky ring, I devised a second experiment (experiment 2, see table 3.1). For each run, I injected the same signal as before, but now forced the Markov chain Monte Carlo code to search for the other parameters while keeping the sky position fixed to either the true values (experiment 2a), or to the sky position in the gap that is labelled by the circle in the first panel of figure 3.2a (experiment 2b). Running the Markov chain Monte Carlo code in this way provides the combination of the free parameters that fits the data best, given the constraint in sky position (the *conditional* posterior distribution, conditional on the corresponding sky position). In particular, the code provides the highest likelihood that can be obtained for this sky position. These likelihoods are listed in table 3.2. They show that the maximum likelihood found in the gap is very similar to the likelihood of the injection for the non-spinning signal, whereas it is significantly lower in the case of the spinning signal. For the non-spinning signal, an unfavourable binary orientation (inclination = 92.0°) and hence a short distance (d_L = 3.6 Mpc) are needed to give a good match for the given sky position (see Section 6.1 for

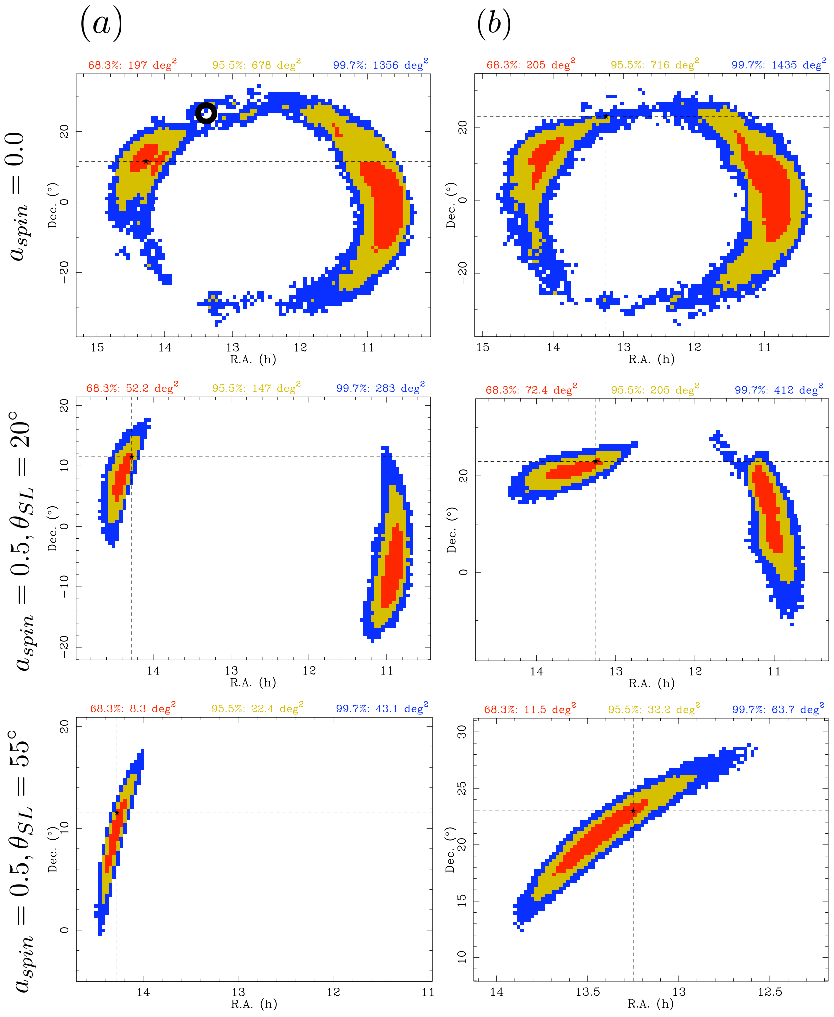

Figure 3.2. Two-dimensional probability-density functions of the sky position for the Markov chain Monte Carlo runs as labelled. The colours show the different probability intervals (1-σ, 2-σ and 3-σ for red, yellow and blue respectively). The black dashed lines mark the position in the sky of the injection for each run. Left column **(a)**: results for the reference runs, experiment 1 (signal injection at R.A. $= 14.3\,$h, Dec $= 11.5°$). The symbol ◯ denotes the "gap" discussed in the text. Right column **(b)**: results for experiment 3: a Markov chain Monte Carlo run with a signal injection at ◯ (R.A. $= 13.25\,$h, Dec $= 23°$). For the non-spinning case, the probability-density functions are very similar to those in the original run, whereas they are very different for the spinning cases (notice the difference in the axis ranges).

Table 3.2. Likelihoods values recovered by the Markov chain Monte Carlo runs of experiment 2b for the sky ring, described in section 3.4.2.

	$a_{\mathrm{spin}} = 0.0$	$a_{\mathrm{spin}} = 0.5$, $\theta_{SL} = 20°$	$a_{\mathrm{spin}} = 0.5$, $\theta_{SL} = 55°$	
network SNR	17.0	18.3	18.4	
$\log(\mathcal{L}(x_a\|\vec{\lambda}_{\mathrm{true}}))$	131	154	208	
$\log(\mathcal{L}_{\max})(\bigcirc)$	131	125	152	
Match $M(h(\vec{\lambda}_{\mathrm{true}}), h(\vec{\lambda}_{\mathcal{L}_{\max}}))$ (equation 1.36)	99.5%	89.6%	82.5%	(between waveforms injected in experiment 1 and those corresponding to $\mathcal{L}_{\max}$)
$\mathcal{L}_{\max}$ parameters :				(reference parameters, injected in experiment 1)
position (R.A. [h], Dec. [°])	13.25, 23	13.25, 23	13.25, 23	14.3, 11.5
orientation (θ_{J_0} [°], ϕ_{J_0} [°])	-65.4, 10.8	-59.5, 340.4	-21.8, 169.5	3.8, 289
inclination ($\arccos(\mathbf{J}\cdot\mathbf{N})$) [°]	92.0	97.5	129.7	128.4
distance [Mpc]	3.7	11.1	18.3	16
$t_{\mathrm{c}}-700009010$ [s]	2.34955	2.34959	2.34960	2.34500

more details). The modulations of the signal due to the precession of the binary orbit prevent this match in the spinning cases.

Thus, for a source with a non-spinning black hole, a high likelihood *can* be found in the gaps of the sky ring. Therefore the absence of high likelihood values does *not* explain the fact that the Markov chains hardly sample this part of the parameter space. Instead, I find that the probability-density functions for some of the other parameters (especially the distance d_{L} and binary orientation $\arccos(\mathbf{J}\cdot\mathbf{N})$) are very narrow for experiment 2b compared to those for experiment 2a (figure 3.3). This indicates that the overall volume of parameter space in these parameters is very small for sky positions in the gap and this is the reason that these gaps are not visited frequently by the chains. On a side note, the priors are flat and can not be the cause for this effect. If the Markov chain Monte Carlo runs had infinite length, they would sample this region in parameter space and bridge the gaps in figure 3.2a with a thin line, *i.e.* the points “bridging” the gaps will form a set of very small measure. Even with a perfect sampling, the same behaviour is to be expected: the chains would mainly sample the arcs and rarely the gaps. Interestingly, the similarity in likelihood values between the true position and the gap for the case of a non-spinning black hole also means that these two signals are virtually indistinguishable, *i.e.* their match (equation 1.36) is very high (99.5% see table 3.2). This indicates that if the source *were* truly in the gap, Markov chains of this length would not recover it, and chains of any length would not have a significant probability-density function in the gaps.

To illustrate this, I did a third experiment (experiment 3, see table 3.1). I injected a signal at the position in the gap labelled by $\bigcirc$ in figure 3.2a. I kept the same masses and spin values as before, and set the other parameters to the values yielding the maximum likelihoods from the second experiment, listed in table 3.2.

In the non-spinning case, the sky ring that is recovered is very similar to that of the original run (see figure 3.2b); the small difference seen can be explained by the fact that the match between the signal injected in experiment 3 and the signal injected in experiment 1 was 99.5%, not 100% (table 3.2). This shows that there exist carefully selected combinations of sky position, binary orientation and distance, which cannot be easily recovered by the analysis (see Section 6.1 for a follow-up solution). However, this reflects a *real* phenomenon; it is very improbable for a source to have the right orientation to produce the gravitational-wave signal I injected *and* have its sky location in the gap. And by giving preference to more likely solutions the parameter-estimation routine is in fact doing the right, completely reasonable thing. The probability-density functions of the relevant parameters for the comparison of experiments 1 and 3 are plotted in figure 3.4.

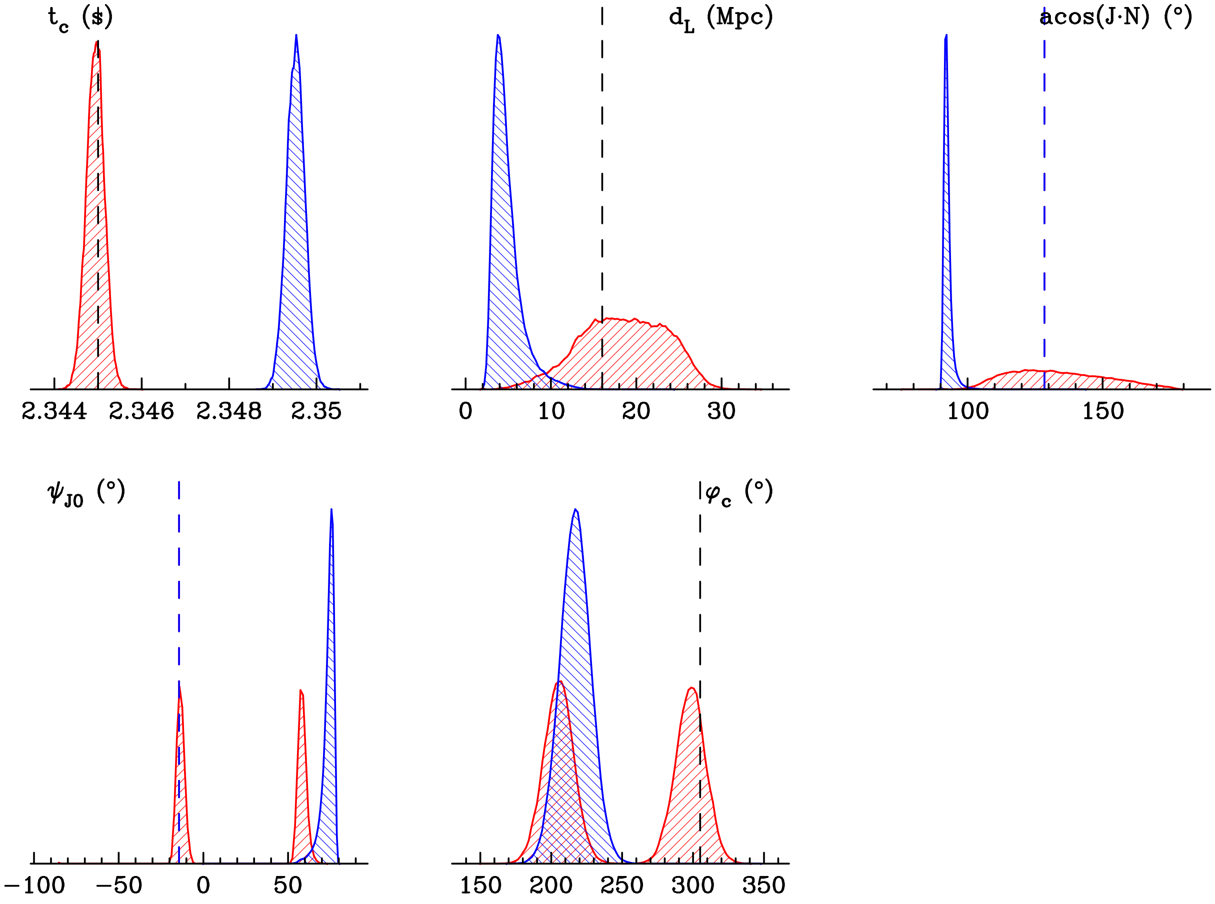

Figure 3.3. One-dimensional probability-density functions for the runs of experiment 2a (red, hatched upward) and of the runs in experiment 2b (blue, hatched downward), in the non-spinning case. The black dashed lines mark the values of the injected parameters. The level of support is indeed smaller in the second case.

The probability-density functions in the other parameters are also very similar in both the original run and the third experiment run.

When the black hole is spinning moderately, the two signals injected in experiment 1 and in experiment 3 are different (as can be inferred from the large difference in likelihood in experiment 2b, and the smaller match, see table 3.2). The different injections yield

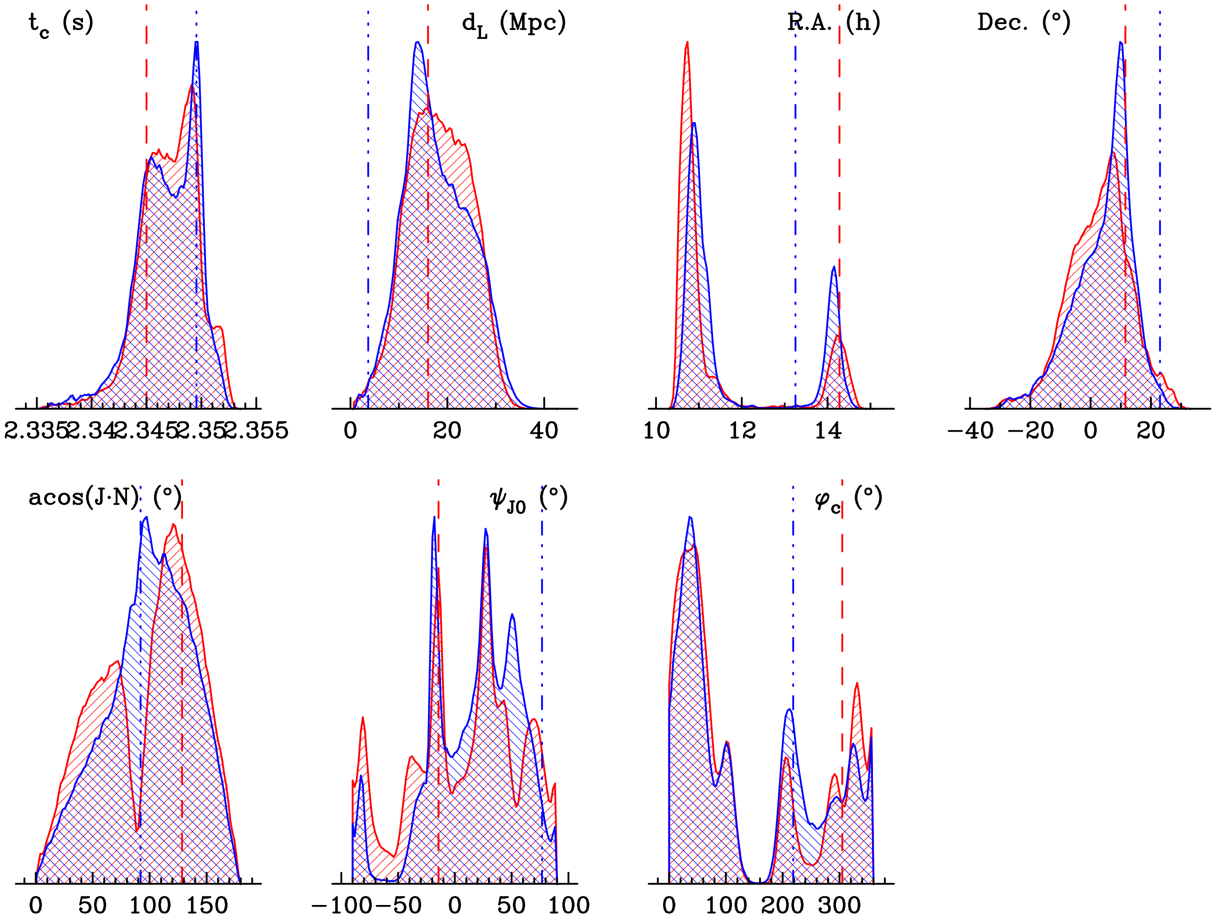

Figure 3.4. One-dimensional probability-density functions for the reference run in experiment 1 (red, hatched from bottom-left to top-right) and of the runs in experiment 3 (blue, hatched from top-left to bottom-right), in the non-spinning case. The dashed lines mark the values of the injected parameters in experiment 1, while the dotted-dashed lines mark the values of the injected parameters in experiment 3. The probability-density functions for all parameters are very similar for the two injections.

significantly different probability-density functions for the sky position (figure 3.2b) as well as for the other parameters, as I checked in the study.

3.4.3. Comparison of Markov chain Monte Carlo runs with 1.5pN and 3.5pN waveforms

So far in this chapter I have used 1.5pN waveforms for computational efficiency. However, in this section I used the Markov chain Monte Carlo implementation to present the first comparison of the accuracy of parameter estimation with the 1.5pN and 3.5pN waveform families, as described in section 3.2. In both cases, I injected black hole-neutron stars binary inspiral waveforms with a non-spinning black hole into the noise of a single interferometer (H1). I analysed the 1.5pN injected waveform with an Markov chain Monte Carlo with 1.5pN waveform templates, and the 3.5pN injected waveform with 3.5pN waveform templates. I scaled the distance to the source to obtain a signal to noise ratio of 20.0 in both cases, which resulted in a distance of $\sim$11.9 Mpc for the 1.5pN waveform case, and $\sim$12.2 Mpc for the 3.5pN waveform case. The remaining injection parameters were set to $a_{\rm spin} = 0.0$, $\mathcal{M} = 3.0M_\odot$, $\eta = 0.11$ ($M_1 = 10.0M_\odot$, $M_2 = 1.4M_\odot$), R.A. = 17.3 h, Dec $= -5^\circ$, $\theta_{J_0} = -23^\circ$, $\phi_{J_0} = 194^\circ$, $\phi_{\rm c} = 352^\circ$ and $t_{\rm c} = 894377000.500244\,{\rm s}$ for this study. The three spin parameters ($a_{\rm spin}$, θ_{SL} and $\alpha_{\rm c}$) were fixed, forcing the chains to explore a parameter space that was effectively 9-dimensional.

Figure 3.5 compares the probability-density functions of the mass parameters for the runs with the 1.5pN and 3.5pN waveforms for $1.5 * 10^6$ iterations in both cases. It is evident that the estimation of the symmetric mass ratio η is more accurate in the 3.5pN case, which results in better constraints on the individual masses. The 2-σ probability ranges for the chirp mass are roughly similar in both cases (a factor of 1.2 narrower when the 3.5pN waveform is used), whereas for η, and hence for the individual masses, the ranges are narrower by a factor of 1.8 when the 3.5pN waveform is used. The additional information in the higher-order post-Newtonian waveforms results in a greater structure of the parameter space. In principle this extra structure allows the estimation of the binary parameters more accurately. However, a more structured parameter space also affects the sampling efficiency of the Markov chain Monte Carlo code negatively, so that more iterations are needed to obtain a well-sampled Markov chain Monte Carlo run. In addition, the computation of a single 3.5pN waveform template takes about 2.4 times longer than that of a 1.5pN template. This effect prevented, for this study, from performing this analysis in a full 12-dimensional or 15-dimensional parameter space in a reasonably short computational time. The code and sampling methods were improved for the work described in the other chapters of this dissertation.

3.5. Conclusions

I have explored the degeneracies in the sky position for a gravitational-wave observation of an inspiral of a black hole-neutron star binary with two non-collocated ground-based interferometers. Whereas simple triangulation based on time delays alone would result in a homogeneous sky ring, the Markov chain Monte Carlo runs show (in experiment 1) an incomplete ring in the sky consisting of arcs separated by gaps. While the arcs make up most of the circumference of the sky ring for an inspiral with a non-spinning black hole, these arcs become smaller when spin is present and may be reduced to a single arc for the case of moderate spin and a sufficient misalignment between the black-hole spin and the orbital angular momentum. I demonstrated that in the spinning case, the maximum likelihood values are in fact lower in the gaps than in the arcs. In the non-spinning case the likelihood in the gaps can actually be as high as in the arcs; however

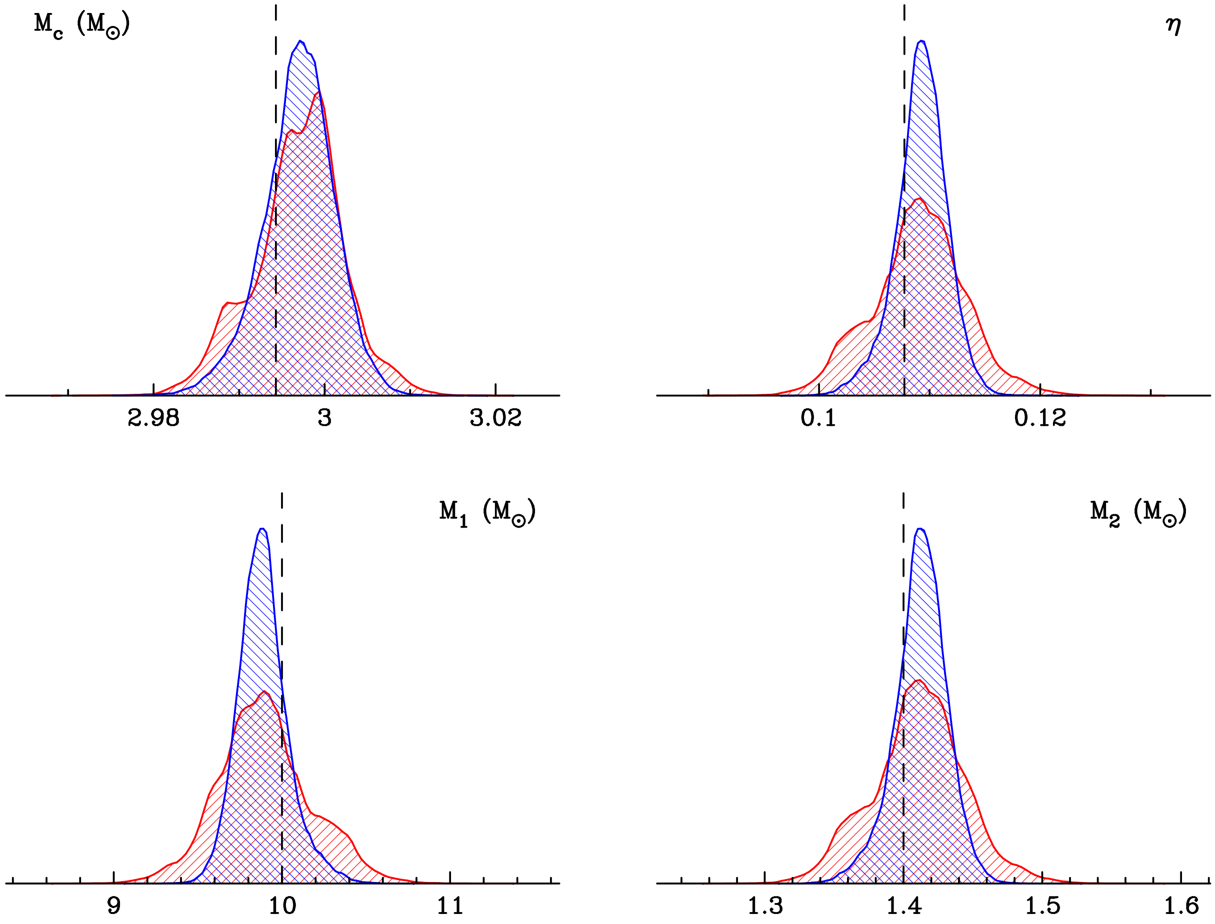

Figure 3.5. probability-density functions from a run with chains starting from the true values, with the 1.5pN waveform (red, hatched from bottom-left to top-right) and the 3.5pN waveform (blue, hatched from top-left to bottom-right) from a non spinning source. Only one detector (LIGO at Hanford) is used.

the gaps can be explained by a smaller volume of support in the other extrinsic parameters, such as the binary orientation and distance (experiment 2). See Section 6.1 for an analytical description and solution. It is then less likely for the chains to sample this smaller volume in parameter space, resulting in gaps in the two-dimensional sky probability density function. In the non-spinning case, if a source is located in a gap, the posterior probability-density function still has a gap at the true source sky location (experiment 3).

The subject of estimating the position of a gravitational-wave source on the sky has been explored by many researchers, in the context of binary-inspiral and burst signals; the assumed baseline for these studies corresponds to three detectors located at the three LIGO-Virgo observatory positions, and operating at their design sensitivities. For detectable burst sources (SNR>5), arrival-time techniques should allow a precision of about 1° for the source direction [62]. A method that takes into account burst-signal arrival time and amplitude, plus arrival-time uncertainties equivalent to what is observed with real LIGO and Virgo data, gives source uncertainties of a few degrees [63]. Coherent techniques also exist for burst detection and sky-location determination, but by their own admission these methods are computationally costly [64]. Many techniques have also been developed for sky localisation for binary-inspiral events. It has been shown, using time and mass parameter estimates, that the LIGO-Virgo network could localize the position of a binary-neutron-star inspiral to an accuracy of 4° if it were located in M87 (16 Mpc), or 2° for a source in NGC 6744 (10 Mpc) [65]; coherent methods, which also depend on estimating the time and mass parameters, give similar accuracies [66].

Markov chain Monte Carlo parameter-estimation methods, like those used in this study, are capable of estimating the sky parameters, along with all of the other signal parameters; this is one reason why Markov chain Monte Carlo methods are computationally intensive. Coherent Markov chain Monte Carlo methods applied to signals observed by the LIGO-Virgo network will be able to resolve the sky location to 2° for signals with an signal-to-noise ratio of 15 [15]. When the compact objects have spin, and the search templates account for this parameter, sky localisation becomes relatively more accurate for higher values of spin [55]. It is important to remember that, in principle, the Markov chain Monte Carlo results show the best constraints one could hope to place on signal parameters (including the sky location) by displaying the true posterior probability-density functions. While comparisons with other particular sky-localisation results may be cumbersome because different waveforms were assumed at different signal-to-noise ratios in different detectors, Markov chain Monte Carlo produced posterior probability-density functions display the statistically correct and most precise localisation. Bayesian methods achieve better parameter-estimation accuracy when the template model describes the functional form of the actual signal more accurately. When a gravitational-wave detection occurs, it is likely that all possible sky localisation algorithms will be used, and the methods should be considered to be complementary.

In section 3.4.3, I compared Markov chain Monte Carlo results on software injections using waveform families of 1.5pN and 3.5pN order for both the injections and the Markov chain Monte Carlo parameter estimation. I have shown that the higher-order templates have the potential for more accurate parameter estimation, but that sampling the parameter space with these templates is more computationally difficult.

CHAPTER 4

Inspiral-Merger-Ringdown effects

4.1. Numerical INJection Analysis

The Numerical INJection Analysis (NINJA, [67]) project is a collaborative effort between members of the numerical relativity and gravitational-wave data analysis communities. The purpose of NINJA is to study the sensitivity of existing gravitational-wave search algorithms using numerically generated waveforms. The first NINJA analysis focused on gravitational waveforms from binary black hole coalescence. Numerical data was used to generate a set of gravitational-wave signals. These signals were injected into a simulated data set, designed to mimic the response of the Initial LIGO and Virgo gravitational-wave detectors. I analysed this data using Markov chain Monte Carlo ([67]). Available numerical relativity signals were of short duration, and at most a few cycles of the inspiral were included. Most of the Signal-to-Noise Ratio (SNR) was included in the merger and ring-down portions of the waveform, for which no signal model was available at the time. This lead to significant biases in the intrinsic parameter recovery. Interestingly, the inspiral-only templates where able to recover the correct timing differences between detectors. As such, the sky location is constrained to an arc of a ring containing the true value.

4.1.1. Analysis methods

I analysed a selection of the injected numerical signals with the Markov chain Monte Carlo code. The signal model was based on waveforms with phase evolution at 1.5 post-Newtonian order and leading-order amplitude evolution (see Section 3.2.1 for more details). Parameter estimation was successful on NINJA injections with relatively low total mass in which the inspiral contained a significant fraction of the total signal-to-noise ratio. For high-mass injections, the algorithm attempted to match the merger and ringdown portions of the injected signal to inspiral templates, resulting in poor parameter estimation.

The post-Newtonian waveforms used in this analysis include the spin of the larger body m_1, allowing us to use the analytical simple-precession waveform [51]. The parameter space thus consists of twelve independent parameters:

$$\vec{\lambda} = \{\mathcal{M}, \eta, \alpha, \delta, \psi, \iota, d, a_{\mathrm{spin}}, \kappa, \phi_{\mathrm{c}}, \alpha_{\mathrm{c}}, t_{\mathrm{c}}\}, \tag{4.1}$$

where $\mathcal{M}$ and η are the chirp mass and symmetric mass ratio, respectively; α (right ascension) and δ (declination) identify the source position in the sky; the angles ψ and ι identify the direction of the total angular momentum of the binary; d is the luminosity distance to the source; $0 \leq a_{\mathrm{spin}} \equiv S_1/m_1^2 \leq 1$ is the dimensionless spin magnitude; κ is the cosine of the angle between the spin and the orbital angular momentum; and ϕ_{c} and α_{c} are integration phase constants that specify the gravitational-wave phase and the location of the spin vector on the precession cone, respectively, at the time of coalescence t_{c}.

The Markov chain Monte Carlo algorithm used for the NINJA analysis was optimised by including a variety of features to efficiently sample the parameter space, such as parallel tempering [16]. This Markov chain Monte Carlo implementation can be run on a data set from a single detector, or on data sets from multiple detectors.

4.1.2. Results

The Markov chain Monte Carlo code was run on a selection of injected signals in the NINJA data. It was found that although the Markov chain Monte Carlo runs are clearly able to detect a signal whenever the inspiral contains a sufficient signal-to-noise ratio, they were unable to correctly determine the signal parameters for many injections. For the high masses typical of most NINJA injections, the signal-to-noise ratio is dominated by the merger and ringdown, so that the inspiral-only templates tried to match the merger and ringdown portions of the injected waveform. Typically, it is found that in such cases the time of coalescence is overestimated since the injected ringdown is matched to an inspiral; the chirp mass is underestimated since the merger/ringdown frequency is higher than the inspiral frequency for a given mass, so that matching them to an inspiral requires the mass to be lower; the mass ratio is underestimated, which allows the waveform to contain more energy in the narrow frequency band corresponding to quasi-normal ringing; and the spin rails against the upper prior of 1 since the innermost stable circular orbit frequency is highest for an inspiral into a maximally-spinning Kerr black hole. I tried to circumvent the problem of matching to the merger and ringdown by introducing more-restrictive priors on spin and/or η. These efforts still failed when the total masses were too high, but were successful in the case of lower total masses and longer inspiral signals.

Figure 4.1 shows the probability density functions produced by runs on an injected equal-mass non-spinning `SpEC` Cornell/Caltech waveform with $\mathcal{M} = 15.6\,M_\odot$. This particular injection was chosen because it had the lowest total mass, and `SpEC` waveforms typically have more inspiral cycles; runs on other injections show comparable results, with the general trend that the higher the total mass (and, thus, the lower the relative fraction of the signal-to-noise ratio contributed by the inspiral), the poorer the parameter estimation becomes.

Data from two detectors, H1 and L1, were used to compute the probability density functions shown in the top row of Figure 4.1. I used wide, flat priors for intrinsic parameters (e.g., $\mathcal{M} \in [2\,M_\odot, 100\,M_\odot]$, $\eta \in [0.03, 0.25]$, $a_{\rm spin} \in [0, 1]$). I find that the values of the intrinsic parameters are not determined very accurately. In particular, the spin rails against the upper bound of 1 while η is underestimated, as expected. I find that the sky location is nevertheless constrained to an arc of a ring containing the true value; the 2-σ ($\sim 95\%$) sky area of the ring shown in the bottom left of Fig. 4.1 is ~ 10000 square degrees.

In the middle row of Fig. 4.1, I plot the probability density functions based on data from three detectors: H1, L1, and V1. The spin parameter was constrained to its true value $a_{\rm spin} = 0$ for this run. This had the effect of forcing the Markov chains to match the inspiral only, significantly improving the resolution of other parameters: for example, the probability density function of η now rails against 0.25, which is its true value. The chirp mass is still somewhat underestimated; a higher signal-to-noise ratio may be necessary to improve the mass determination. Promisingly, it was found that the sky location is constrained to a smaller patch on the sky: the 2-σ sky area in the bottom right of Fig. 4.1

is 6300 square degrees. In fact, the sky localisation is even better when the spin parameter is allowed to vary, allowing the Markov chain Monte Carlo to use the signal-to-noise ratio contributed by the ringdown; removing the spin-parameter constraint reduces the 2-σ sky area to 2750 square degrees. This ability to determine the source position will be significant in any future searches for electromagnetic counterparts of gravitational-wave triggers.

The next instance of the NINJA project, NINJA-2 will feature hybridised waveforms, where a numerical relativity waveform is made longer by attaching early inspiral cycle from post-Newtonian calculations. NINJA-2 is well on its way and I expect much better results on those longer waveforms, with the added improvement of being able to use waveform models for parameter estimation containing a prescription for merger and ringdown.

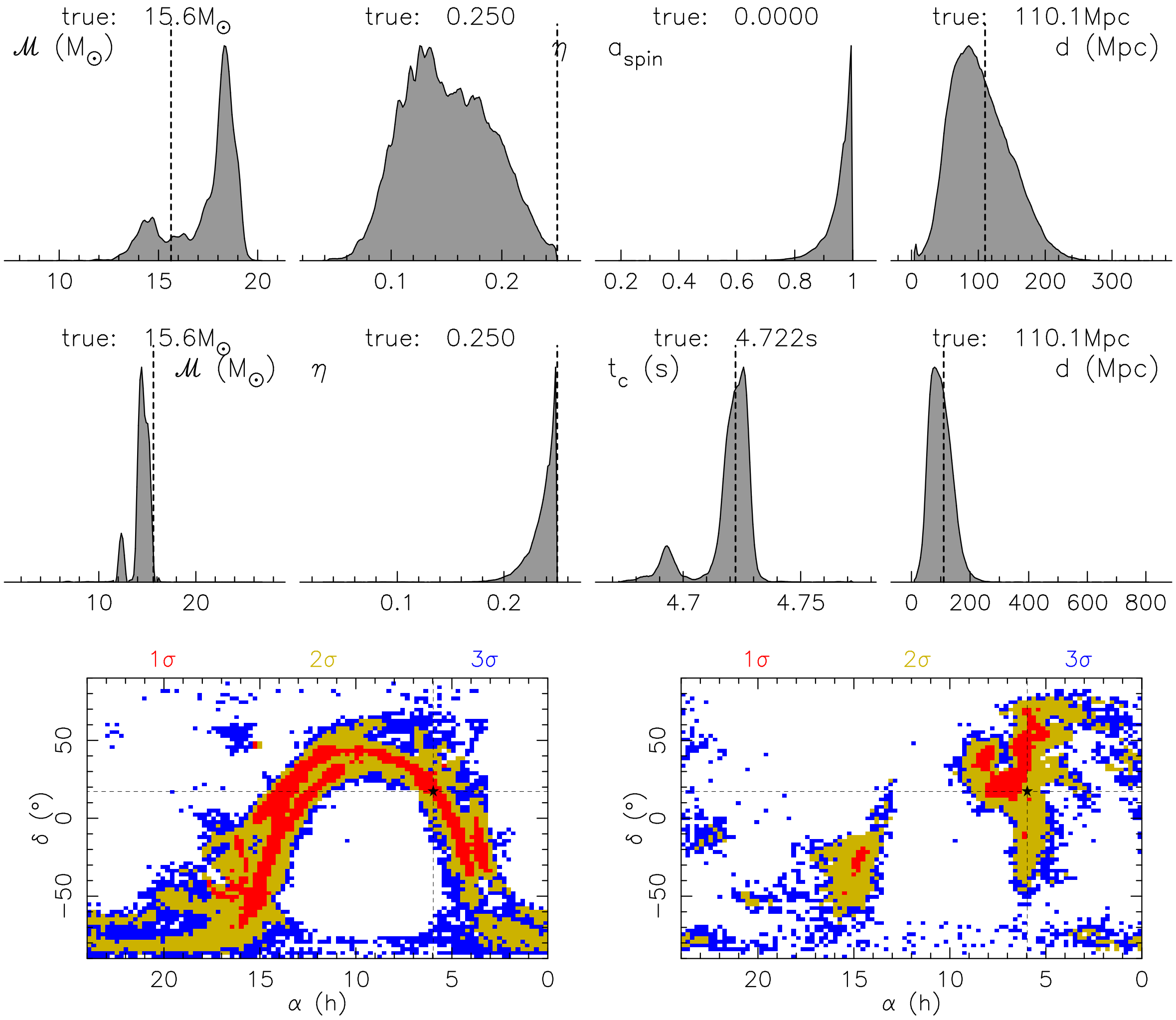

Figure 4.1. Results of the Markov chain Monte Carlo analysis for one of the injected NINJA waveforms. The top row shows the marginalised probability density functions for $\mathcal{M}$, η, a_{spin}, and d produced by a two-detector Markov chain Monte Carlo analysis on an injected non-spinning equal-mass `SpEC` Cornell/Caltech waveform (true values $\mathcal{M} = 15.6\,M_{\odot}$, $\eta = 0.25$, $t_{\text{c}} = 4.7223\,\text{s}$, and $a_{\text{spin}} = 0$). Middle row: the same probability density functions (but with a_{spin} replaced by t_{c}) for a three-detector run with constrained spin on the same injection. Bottom row: two-dimensional probability density functions for the sky position with the 2-detector run on the left and the three-detector Markov chain Monte Carlo run on the right; the 1-σ, 2-σ and 3-σ probability areas are displayed in different colours, as indicated in the top of each panel. Dashed lines denote the true values of injected parameters.

CHAPTER 5

The effects of LIGO detector noise on a 15-dimensional Markov chain Monte Carlo analysis of gravitational-wave signals

I present in this chapter parameter-estimation results on signals from binaries with precessing spins. Two data sets are created by injecting simulated gravitational-wave signals into either synthetic Gaussian noise or into LIGO detector data. I compute the 15-dimensional probability-density functions (PDFs) for both data sets, as well as for a data set containing LIGO data with a known, loud artefact ("glitch"). I show that the analysis of the signal in detector noise yields accuracies similar to those obtained using simulated Gaussian noise. I also find that while the Markov chains from the glitch do not converge, the probability-density functions would look consistent with a gravitational-wave signal present in the data. While the parameter-estimation results are encouraging, further investigations into how to differentiate an actual gravitational-wave signal from noise are necessary.

5.1. Introduction

The detection of a gravitational-wave event is challenging and will be a rewarding achievement by itself. After such a detection, measurement of source properties holds major promise for improving our astrophysical understanding and requires reliable methods for parameter estimation. This is a complicated problem, because of the large number of parameters (15 for spinning compact objects in a quasi-circular orbit) and the degeneracies between them, see Section 3.4.2, [8], the significant amount of structure in the parameter space, and the particularities of the detector noise.

In this section I use an example to illustrate the capabilities of the algorithm on the effects of using LIGO detector data versus synthetic Gaussian noise.

In section 5.3.1 I describe the three data sets that I analyse in this study; a simulated gravitational-wave signal injected into synthetic Gaussian noise, a gravitational-wave signal injected into LIGO detector data and a raw LIGO data set containing a known artefact of terrestrial origin ("glitch"). I describe the details of the Markov chain Monte Carlo simulations in section 5.3.2. The analyses of the first two data sets are compared in section 5.3.3, and I present results on the glitch in section 5.3.4.

5.2. Gravitational-wave signal and observables

I analyse the signal produced during the inspiral phase of two compact objects of masses $M_{1,2}$ in quasi-circular orbit. I focus on a black-hole binary system with $M_1 = 10\,\mathrm{M}_\odot$ and $M_2 = 1.4\,\mathrm{M}_\odot$, where I do not ignore the second spin in order to explore the single spin approximation. During the orbital inspiral, the general-relativistic spin-orbit and spin-spin coupling (dragging of inertial frames) cause the binary's orbital plane to precess and introduce amplitude and phase modulations of the observed gravitational-wave signal [51].

A circular binary inspiral with both compact objects spinning is described by a 15-dimensional parameter vector $\vec{\lambda} \in \Lambda$. My choice of independent parameters with respect to a fixed geocentric coordinate system is:

$$\vec{\lambda} = \{\mathcal{M}, \eta, \log d_{\rm L}, t_{\rm c}, \phi_{\rm c}, \alpha, \cos\delta, \sin\iota, \psi,$$

$$a_{\rm spin1}, \cos\theta_{\rm spin1}, \phi_{\rm spin1}, a_{\rm spin2}, \cos\theta_{\rm spin2}, \phi_{\rm spin2}\}, \tag{5.1}$$

where $\mathcal{M} = \frac{(M_1 M_2)^{3/5}}{(M_1+M_2)^{1/5}}$ and $\eta = \frac{M_1 M_2}{(M_1+M_2)^2}$ are the chirp mass and symmetric mass ratio, respectively; $d_{\rm L}$ is the luminosity distance to the source; $\phi_{\rm c}$ is an integration constant that specifies the gravitational-wave phase at the time of coalescence $t_{\rm c}$, defined with respect to the centre of the Earth; α (right ascension) and δ (declination) identify the source position in the sky; ι defines the inclination of the binary with respect to the line of sight; and ψ is the polarisation angle of the waveform. The spins are specified by $0 \leq a_{{\rm spin}_{1,2}} \equiv S_{1,2}/M_{1,2}^2 \leq 1$ as the dimensionless spin magnitude, and the angles $\theta_{\rm spin1,2}$,$\phi_{\rm spin1,2}$ for their orientations. The parameter priors are uniform in the parameters of Eq. 5.1.

The waveform used includes terms up to 3.5-post-Newtonian (pN) order in phase and uses Newtonian amplitudes, with spin effects up to 2.5pN in phase. I generate the waveform templates using the routine `LALGenerateInspiral()` with the approximant `SpinTaylor` from the injection package in the LSC Algorithm Library (LAL) [56], which closely follows the first section of [45].

5.3. Parameter estimation: Results

5.3.1. Data sets

For this chapter, I analyse three different data sets, each containing the data for the 4-km LIGO detectors at Hanford (H1) and Livingston (L1):

DS1:: a coherent software injection with a total signal-to-noise ratio of 11.3 into synthetic Gaussian, stationary noise, simulated for the H1 and L1 detectors;

DS2:: a coherent software injection of the same signal, with a total signal-to-noise ratio of 11.3, into "quiet" LIGO detector data from H1 and L1;

DS3:: raw LIGO data from H1 and L1, containing a known, coincident glitch of seismic origin, with a total signal-to-noise ratio of 11.3.

For the data sets DS1 and DS2, the injected signal is that of a $10\,M_\odot$ spinning black hole and a $1.4\,M_\odot$ spinning neutron star in an inspiralling binary system. A low-mass Compact Binary Coalescence Group search [68] does not produce a gravitational-wave trigger for the data segment DS2; hence I designate it "quiet". The distance of each of the injections is scaled to obtain an signal-to-noise ratio of 11.3, equal to that of the glitch in DS3, but computed with different waveforms: a SpinTaylor waveform (see section 5.2) for DS1 and DS2, and a non-spinning, 2pN waveform (see section 5.3.4) for DS3. The other parameters of the injection are:

$$\begin{aligned}\vec{\lambda} = \; & \{\mathcal{M} = 2.99\,M_\odot, \eta = 0.107, d_{\mathrm{L}}, t_{\mathrm{c}}, \phi_{\mathrm{c}} = 85.9^\circ, \alpha = 17.4\,h, \delta = 61.6^\circ, \\ & i = 52.8^\circ, \psi = 11.6^\circ, a_{\mathrm{spin1}} = 0.6, \theta_{\mathrm{spin1}} = 78.5^\circ, \phi_{\mathrm{spin1}} = 63.0^\circ, \\ & a_{\mathrm{spin2}} = 0.4, \theta_{\mathrm{spin2}} = 120.0^\circ, \phi_{\mathrm{spin2}} = 315.1^\circ\}, \end{aligned} \tag{5.2}$$

where I assigned a spin of 0.4 to the neutron star, which is higher than astrophysically plausible, for testing purposes only. In DS3, no signal is injected. For those analyses, I use the data of both 4-km LIGO detectors H1 and L1.

5.3.2. Markov chain Monte Carlo simulations

The Markov chain Monte Carlo analysis that I carry out on each data set consists of 10 independent Markov chains, each with a length of about a million iterations and composed of 5 chains at different temperatures for parallel tempering. From now on, I will refer to the $T = 1$ chain as *the chain*, since the hotter chains were not used in the post-processing. The part of the chains that is analysed is that after the *burn-in* period [**17**]see *e.g.*, the length of which is determined automatically as follows: I determine the absolute maximum likelihood $\log(\mathcal{L}_{\rm max})$, defined as the highest value for $\log[p(\vec{x}|\vec{\lambda}, M)]$ obtained over the ensemble of parameter sets $\vec{\lambda}$ in any of the individual Markov chains. Then for each chain I include all the iterations *after* the chain reaches a likelihood value of $\log(\mathcal{L}_{\rm max}) - 2$ for the first time. This results in a convergence test as well, since some of the independent chains may not reach this threshold value. Typically, I demand that more than 50% of the chains meet this condition before I consider the Markov chain Monte Carlo run as *converged*, although I consider results as *robust* if they have a convergence rate of 80% or more. This convergence test is a measure of the quality of the sampling in a given number of iterations. All the Markov chains start at values that are randomly offset from the injection values. The starting values for $\mathcal{M}$ and $t_{\rm c}$ are drawn from a Gaussian distribution centred on the injection value, with a standard deviation of $0.025\,M_{\odot}$ and 10 ms respectively. In real analysis, the two Gaussian distributions are centred on the values from the template bank based search of the Compact Binary Coalescence group [**68**], which will have triggered the Markov chain Monte Carlo followup. The other thirteen parameters are drawn uniformly from their allowed ranges.

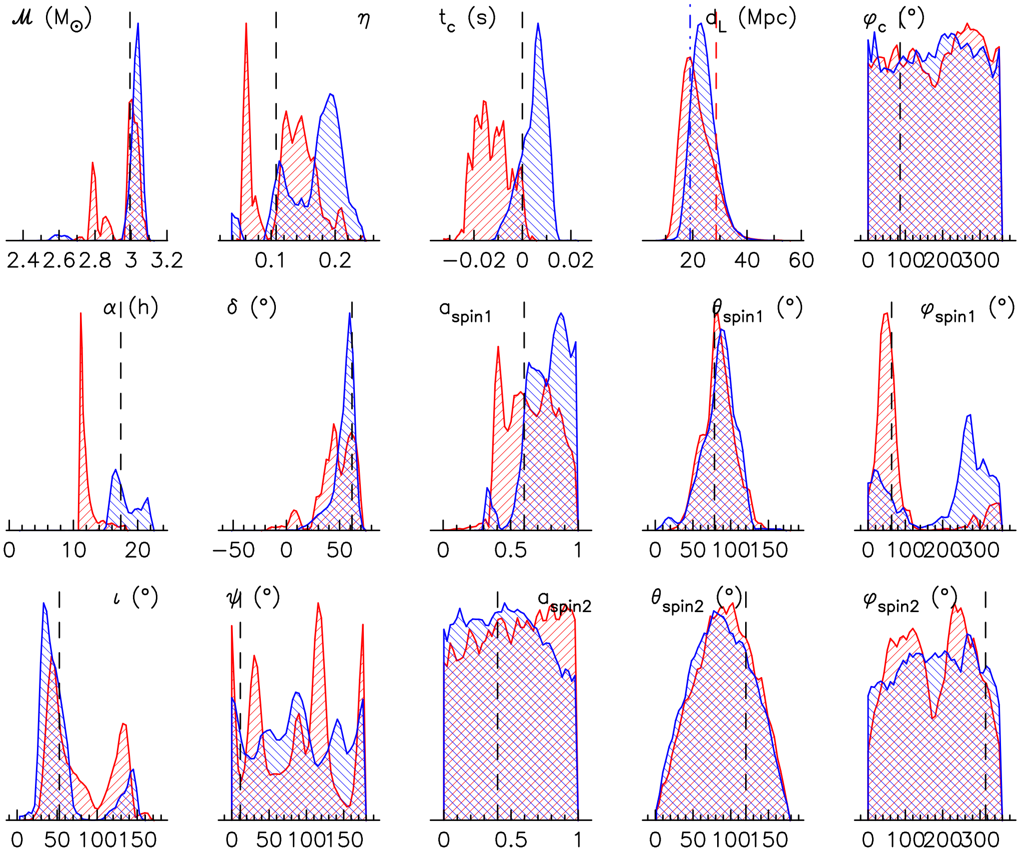

Figure 5.1. One-dimensional marginalised probability density functions for all 15 parameters from the analysis of data sets DS1 (hatched upward; red in the online colour version) and DS2 (hatched downward; blue in the online colour version). The vertical dashed lines mark the injection values.

5.3.3. Analysis of data sets DS1 and DS2

I analysed the data sets DS1 and DS2 as described in section 5.3.1 and the results of both analyses passed the convergence test described in section 5.3.2 with convergence rates of 70% and 80%, respectively. The resulting one-dimensional marginalised probability density functions from both analyses are shown in figure 5.1.

Table 5.1 shows the median and the width of the 95%-probability ranges for each parameter. The differences I find between the results for DS1 and DS2 are attributed

Table 5.1. Median and width of the 95%-probability ranges for each parameter of the analyses of data sets DS1 and DS2. The column *recovered* indicates whether or not the 95% range includes the injection value.

		DS1 (synthetic noise)			DS2 (detector noise)		
	injection	median	95% width	recovered	median	95% width	recovered
$\mathcal{M}\,(M_\odot)$	2.99	3.006	0.294	yes	3.041	0.122	yes
η	0.107	0.133	0.145	yes	0.183	0.144	yes
$d_\mathrm{L}\,(\mathrm{Mpc})$	28.615	21.240	20.764	yes	24.144	17.238	yes
$t_\mathrm{c}\,(\mathrm{s})$	0.000	-0.013	0.024	yes	0.006	0.019	yes
$\phi_\mathrm{c}\,(^\circ)$	85.944	189.745	342.398	yes	185.482	343.175	yes
$\alpha\,(\mathrm{h})$	17.380	11.684	5.349	**no**	17.786	6.320	yes
$\delta\,(^\circ)$	61.642	49.326	64.346	yes	58.390	39.796	yes
$i\,(^\circ)$	52.753	67.056	110.735	yes	46.850	122.787	yes
$\psi\,(^\circ)$	11.459	93.162	176.358	yes	88.706	173.869	yes
a_spin1	0.600	0.658	0.594	yes	0.804	0.478	yes
$\theta_\mathrm{spin1}\,(^\circ)$	78.463	85.490	83.110	yes	89.225	85.787	yes
$\phi_\mathrm{spin1}\,(^\circ)$	63.025	57.171	335.592	yes	263.014	345.700	yes
a_spin2	0.400	0.532	0.945	yes	0.475	0.940	yes
$\theta_\mathrm{spin2}\,(^\circ)$	120.000	94.687	150.544	yes	89.406	146.101	yes
$\phi_\mathrm{spin2}\,(^\circ)$	315.127	181.959	327.603	yes	184.681	339.071	yes
$M_1\,(M_\odot)$	10.002	8.533	8.849	yes	6.421	6.536	yes
$M_2\,(M_\odot)$	1.400	1.598	1.277	yes	2.036	1.564	yes

to the particular noise realisations in this example, and most parameters yield similar probability density functions and accuracies.

The probability density functions of the parameters that describe the spin of the NS follow the prior distributions in both runs. This justifies ignoring the NS spin (by fixing a_spin2 to 0.0 in the recovery template) for this mass ratio, as in Section 3.2. For each of the two data sets, DS1 and DS2, I computed the Bayes factor to compare the evidence for the following two models using the harmonic-mean method, see Section 1.2.4, Eq. 1.49: M_1: a 3.5pN inspiral waveform embedded in Gaussian noise, and M_2: Gaussian noise only. The values are listed in table 5.2. In both cases, the Bayes factor is large, providing strong evidence for a gravitational-wave signal in the data. The difference in Bayes factor between

Table 5.2. Bayes factors $B_{1,2}$ between the models M_1: a 3.5pN inspiral waveform embedded in Gaussian noise, and M_2: Gaussian noise only (section 5.3.3) for data sets DS1 and DS2 (see section 5.3.1).

	DS1 (Gaussian noise)	DS2 (detector data)	DS3 (glitch)
$\log_e B_{1,2}$	52.9	43.5	68.5

DS1 and DS2 is attributed to an inherent spread due to different noise realisations, and the uncertainties of the method to estimate the Bayes factor (Section 1.2.4). The results in this section show an illustrative example, but cannot be used to draw firm conclusions. However, it is clear that they warrant a larger, systematic study of these phenomena with the methods described here.

5.3.4. Analysis of data sets DS2 and DS3

On November 2nd 2006, seismic activity at Hanford and Livingston resulted in a coincident "glitch" in the data from the H1 and L1 LIGO detectors. These glitches were recovered by the Compact Binary Coalescence detection pipeline at an signal-to-noise ratio of 11.3, using non-spinning, stationary-phase-approximation templates, Newtonian in amplitude and 2.0pN in phase [68]. I defined the corresponding data set as DS3 in section 5.3.1 and analysed the data as if it had yielded a gravitational-wave trigger. The convergence test from section 5.3.2 yields a 20% convergence rate, which results in the rejection of the results as *not converged*. However, when I nevertheless construct the marginalised one-dimensional probability density functions from the data of the two converged chains (because of the small number of data points, the resulting probability density functions may not be very accurate), they are similar in appearance to those from DS2 (see figure 5.2). The Bayes factors in table 5.2 even suggest that the data set DS3

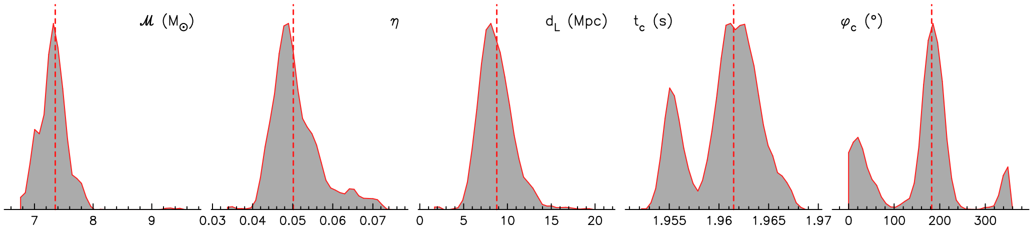

Figure 5.2. One-dimensional marginalised probability density functions of a few selected parameters from the analysis of data set DS3. The vertical dashed lines indicate the median of each probability density function.

is more consistent with containing a gravitational-wave signal than DS2 (with the caveat that the signal-to-noise ratios of DS2 and DS3 were not computed the same way). On the other hand, the low value for the median of η (0.05) corresponds to a mass ratio of 18, which is near the limit of the regime where post-Newtonian expansions are valid. In particular, a small value for eta suggests a slow frequency evolution which may indicate a spike in the frequency spectrum that dominates the signal. In addition, I find that the sky map for DS3 does not display the (parts of a) sky ring that is expected for an analysis using two non-co-located detectors, see Section 3.4.2, [8].

5.4. Conclusions

I presented an example of the analysis of software injections into both simulated Gaussian noise (DS1) and LIGO-detector data (DS2). I also presented an analysis of a data set containing no injection, but a “glitch” coincident in two LIGO interferometers (DS3). These examples demonstrate a remarkable similarity between the results obtained from a gravitational-wave signal injected in Gaussian noise and a similar signal in detector data. The Bayes factors are also similar, where it is to be noted that the harmonic mean technique for computing the Bayes factor yields estimates with significant variance, and more precise estimates are possible, see Section 1.2.4. In addition, I find that although the Markov chains in the analysis of a coincident glitch in LIGO data do not converge, the resulting probability density functions could look remarkably consistent with a simulated gravitational-wave signal. I plan to run the code on a very large number of coincident triggers from the LIGO Compact Binary Coalescence search pipeline (noise events that are somehow being registered as resembling a binary inspiral) in order to get a good sense of how to distinguish them from actual inspirals. The upcoming Engineering Run 2 organised by the LIGO-Virgo collaboration is a very good venue for such a campaign.

CHAPTER 6

Physically motivated exploration of parameter space

6.1. Extrinsic parameter exploration

6.1.1. Degeneracies

As discussed in Section 3.4.2, there exists a near-degeneracy in the detector response to a gravitational wave involving the sky location, hour angle α, declination δ, and polarization, ψ, of the source when three non-collocated detectors are used. In the following discussion I will restrict myselves to the case of non-spinning signals for simplicity. Some of my approximations are inapplicable to spinning signals, but I expect that my jump proposal may still prove useful in the spinning case, particularly for signals that are weak.

The reflection of the true location of the source through the plane defined by the three detectors conserves the arrival time at each detector. This is the reason why in most three-detector analyses, two modes in the sky location are recovered, see Fig. 6.1 (top left). The reflection condition keeps the arrival time of the signal at each detector, Δ_1, Δ_2 and Δ_3, with $\Delta_i(\alpha, \delta, t_c)$, given by:

$$\Delta_i(\alpha, \delta) = S \cdot (-L_i) + t_c \tag{6.1}$$

constant. Here the detector location is labelled by the vector L_i, and the source by the vector $S(\alpha, \delta)$:

$$S(\alpha,\delta) = \begin{pmatrix} \cos\alpha\,\cos\delta \\ -\sin\alpha\,\cos\delta \\ \sin\delta \end{pmatrix} \tag{6.2}$$

This degeneracy artificially includes the time parameter t_c as well, since the reference time is at geocentre and the plane of the detectors does not in general include the centre of the Earth.

This particular degeneracy has been well documented and a jump proposal has been implemented involving the sky location and the reference time, see for instance [**13**]. However, the detector network sensitivity pattern is not uniform on the sky. Any change in sky location will change the effective strength of the model template in each detector, and changes in polarization, inclination and distance are needed to compensate. Both sky positions in Fig. 6.1 (top left) correspond to different values of polarization, inclination and distance. The top right plot shows the same blobs in the distance-inclination space, and the bottom left the correlation between right ascension and distance. Note that on the other hand, intrinsic parameters like masses $m_{1,2}$ do not correlate with those multidimensional blobs as illustrated in the bottom right plot for the chirp-mass $\mathrm{Mc} = \frac{(m_1 m_2)^{3/5}}{(m_1+m_2)^{1/5}}$.

6.1.2. Equations

The signal h is the sum of two polarisations (in the non-spinning case):

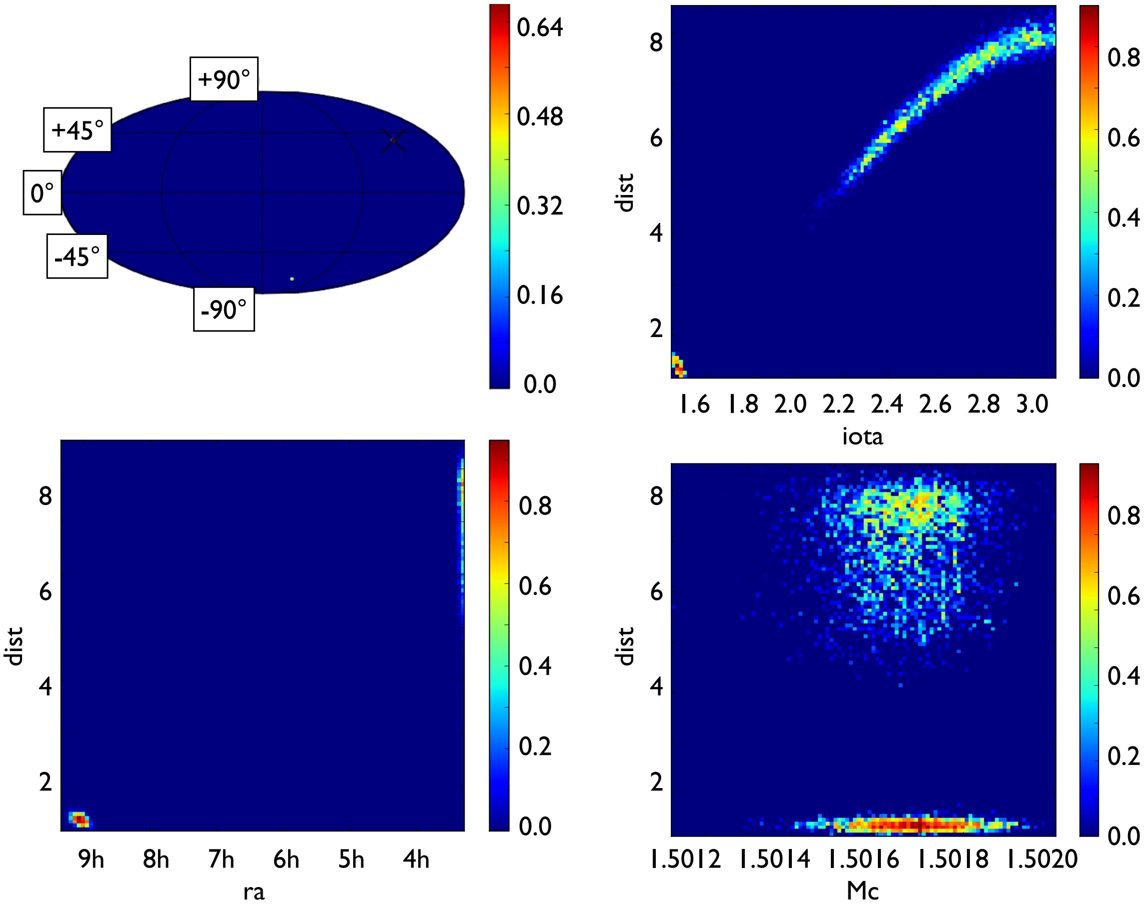

Figure 6.1. Simulation of a parameter recovery analysis. The injected signal was a post-Newtonian non-spinning binary neutron star ($m_1 = 1.8\,\mathrm{M}_\odot$, $m_2 = 1.6\,\mathrm{M}_\odot$) at a signal-to-noise ratio of 40, recovered with a post-Newtonian frequency-domain non-spinning template model. Top left: two dimensional probability density function in right ascension and declination. The black cross marks the injected values. Two spots in the sky show a high probability in this map. Top right: two dimensional probability density function in inclination and distance. Each blob corresponds to one of the blobs in the top left figure. Bottom left: two dimensional probability density function in distance and right ascension. Each blob corresponds to one of the blobs in the top left figure. Bottom right: two dimensional probability density function in chirp mass and distance. Each blob corresponds to one of the blobs in the top left figure.

$$h = F_+(\alpha, \delta, \psi) H_+(m_1, m_2, \iota, \phi, d, t_c) + F_\times(\alpha, \delta, \psi) H_\times(m_1, m_2, \iota, \phi, d, t_c) \tag{6.3}$$

Where the antenna beam pattern functions of the detectors $F_{+,\times}(\alpha, \delta, \psi)$, (see Eq. 1.13), are functions of the hour-angle α (right ascension corrected for the earth's rotation), the declination δ and polarisation angle ψ of the source. They are also parameterised by t_c and the detector three dimensional 2nd-order response tensor D. I recall here their general form as a function of the polarisation angle ψ:

$$F_{i+}(\alpha, \delta, \psi) = x_i(\alpha, \delta)\ \cos(2\psi) + y_i(\alpha, \delta)\ \sin(2\psi) \tag{6.4}$$

$$F_{i\times}(\alpha, \delta, \psi) = y_i(\alpha, \delta)\ \cos(2\psi) - x_i(\alpha, \delta)\ \sin(2\psi) \tag{6.5}$$

Where the functions $x_i(\alpha, \delta)$ and $y_i(\alpha, \delta)$ are complicated functions of the sky location.

The waveform polarisations $H_{+,\times}(m_1, m_2, \iota, \phi, d, t_c)$ are functions of the masses $m_{1,2}$, the inclination ι (angle between the line of sight and the orbital angular momentum), the phase at a reference time (usually either time at coalescence or time at the start of the template generation) ϕ, the distance to the observer d and the time at coalescence t_c. And they can be written in the non-spinning case, considering only the dominant 2-2 mode, as:

$$H_+(m_1, m_2, \iota, \phi, d, t_c) = -\frac{1+\cos^2(\iota)}{2\,d} H_+(m_1, m_2, \phi) \tag{6.6}$$

$$H_\times(m_1, m_2, \iota, \phi, d, t_c) = \frac{\cos\,\iota}{d} H_\times(m_1, m_2, \phi) \tag{6.7}$$

Abusing notations, from now on $H_{+,\times}$ refers to $H_{+,\times}(m_1, m_2, \phi)$, and I omit t_c which provides an overall sliding of the waveform (but enters the equation due to our definition of right ascension and time being at geocentre). I define now the two quantities of interest:

$$A_{i+}(\alpha, \delta, \psi, \iota, d) = -\frac{1+\cos^2(\iota)}{2\,d} F_{i+}(\alpha, \delta, \psi) \tag{6.8}$$

$$A_{i\times}(\alpha, \delta, \psi, \iota, d) = \frac{\cos\,\iota}{d} F_{i\times}(\alpha, \delta, \psi) \tag{6.9}$$

To keep the detector response exactly fixed under a change of parameters, we want to have for each detector:

$$A_{i+}(\alpha, \delta, \psi, \iota, d) = A_{i+}(\alpha', \delta', \psi', \iota', d') \tag{6.10}$$

$$A_{i\times}(\alpha, \delta, \psi, \iota, d) = A_{i\times}(\alpha', \delta', \psi', \iota', d') \tag{6.11}$$

And:

$$\Delta(\alpha, \delta, t_c) = \Delta(\alpha', \delta', t_c') \tag{6.12}$$

There are 6 independent variables, with a total of 3 constraints for a 1 detector network, 6 constraints for a 2 detector network and 9 constraints for a 3 detector network.

Using the Quadrupole approximation, and to keep the same likelihood values, I will try to keep the amplitude of the signal constant for each detector i:

$$R_i^2 = A_{i+}^2 + A_{i\times}^2 \tag{6.13}$$

constant. This gives in the 3 detector network three additional constraints to the time delay constraints, and leads to a system of 6 equation and 6 variables. The solutions form a set of measure zero as expected, see for instance the narrow blobs (no lines nor extended surfaces) in Fig. 6.1. (The posterior distribution is composed of two blobs instead of two points because of the finite signal-to-noise ratio.)

6.1.3. Solution

Starting from a set of parameters $\alpha, \delta, t_c, \psi, \iota, d$, we want to compute a new set $\alpha', \delta', t_c', \psi', \iota', d'$, which conserves Eq. 6.13 and satisfies Eq. 6.12. We compute the R_i^2 from Eq. 6.13. Using only Eq. 6.12 for each of the three detectors gives the new values α', δ', t_c' from geometric arguments. The procedure consists of reflecting the sky position across the plane of the detectors and computing the corresponding t_c. This procedure is described in the literature, see for instance [13] and references therein.

We know have the values of α', δ', t_c' and:

$$F_{i+}(\alpha', \delta', \psi') = x_i(\alpha', \delta')\ \cos(2\psi') + y_i(\alpha', \delta')\ \sin(2\psi') = F'_{i+}(\psi') \tag{6.14}$$

$$F_{i\times}(\alpha', \delta', \psi') = y_i(\alpha', \delta')\ \cos(2\psi') - x_i(\alpha', \delta')\ \sin(2\psi') = F'_{i\times}(\psi') \tag{6.15}$$

In practice to determine the values of x'_i and y'_i, I just use:

$$F_{i+}(\alpha', \delta', 0) = x_i(\alpha', \delta') \tag{6.16}$$

$$F_{i\times}(\alpha', \delta', 0) = y_i(\alpha', \delta') \tag{6.17}$$

We can now write:

$$R_i^2 = A_{i+}^2 + A_{i\times}^2 = \left(-\frac{1+\cos^2(\iota')}{2\,d} F'_{i+}(\psi')\right)^2 + \left(\frac{\cos\ \iota'}{d} F'_{i\times}(\psi')\right)^2 \tag{6.18}$$

I arbitrarily choose detectors 1 and 2 to write:

$$\frac{R_1^2}{R_2^2} = \frac{\left(1+\cos^2(\iota')\right)^2 F'_{1+}(\psi')^2 + 4\left(\cos\ \iota'\right)^2 F'_{1\times}(\psi')^2}{\left(1+\cos^2(\iota')\right)^2 F'_{2+}(\psi')^2 + 4\left(\cos\ \iota'\right)^2 F'_{2\times}(\psi')^2} \tag{6.19}$$

And detectors 2 and 3 to write:

$$\frac{R_2^2}{R_3^2} = \frac{\left(1+\cos^2(\iota')\right)^2 F'_{2+}(\psi')^2 + 4\left(\cos\ \iota'\right)^2 F'_{2\times}(\psi')^2}{\left(1+\cos^2(\iota')\right)^2 F'_{3+}(\psi')^2 + 4\left(\cos\ \iota'\right)^2 F'_{3\times}(\psi')^2} \tag{6.20}$$

Eq. 6.19 can be solved for $(cos\, \iota)^2$ to give:

$$(\cos\ \iota')^2 = \frac{R_1^2\left(2F'_{2\times}(\psi')^2 + F'_{2+}(\psi')^2\right) - R_2^2\left(2F'_{1\times}(\psi')^2 + F'_{1+}(\psi')^2\right)}{F'_{1+}(\psi')^2R_2^2 - F'_{2+}(\psi')^2R_1^2} \\ - 2\sqrt{\frac{\left(F'_{2\times}(\psi')^2R_1^2 - F'_{1\times}(\psi')^2R_2^2\right)}{\left(F'_{2+}(\psi')^2R_1^2 - F'_{1+}(\psi')^2R_2^2\right)^2}} \\ \times\sqrt{\frac{\left(R_1^2\left(F'_{2\times}(\psi')^2 + F'_{2+}(\psi')^2\right) - R_2^2\left(F'_{1\times}(\psi')^2 + F'_{1+}(\psi')^2\right)\right)}{\left(F'_{2+}(\psi')^2R_1^2 - F'_{1+}(\psi')^2R_2^2\right)^2}} \tag{6.21}$$

Plugging this solution into Eq. 6.20 gives the equation for ψ', simple linear equation of $\cos(4\psi')$ and $\sin(4\psi')$:

$$0 = (R_3^2x_2^2y_1^2 - R_2^2x_3^2y_1^2 - R_3^2x_1^2y_2^2 + R_1^2x_3^2y_2^2 + R_2^2x_1^2y_3^2 - R_1^2x_2^2y_3^2)\cos(4\psi') \\ + (-R_3^2x_1x_2^2y_1 + R_2^2x_1x_3^2y_1 + R_3^2x_1^2x_2y_2 - R_1^2x_2x_3^2y_2 + R_3^2x_2y_1^2y_2 \\ - R_3^2x_1y_1y_2^2 - R_2^2x_1^2x_3y_3 + R_1^2x_2^2x_3y_3 - R_2^2x_3y_1^2y_3 + R_1^2x_3y_2^2y_3 \\ + R_2^2x_1y_1y_3^2 - R_1^2x_2y_2y_3^2)\sin(4\psi') \tag{6.22}$$

Which I rewrite:

$$0 = a\cos(4\psi') + b\sin(4\psi') \tag{6.23}$$

And the solution is then:

$$\psi' = \frac{1}{2}\arctan\left(\frac{b - a\sqrt{\frac{a^2+b^2}{a^2}}}{a}\right)$$

or

$$\psi' = \frac{1}{2}\arctan\left(\frac{b + a\sqrt{\frac{a^2+b^2}{a^2}}}{a}\right) \tag{6.24}$$

Only one of the two solutions of Eq. 6.24 when plugged into Eq. 6.22 satisfy $0 \geq \cos(\iota')^2 \leq 1$.

The distance d' can be computed using Eq. 6.13 for any given detector:

$$d' = \frac{\sqrt{\left(\frac{1+\cos^2(\iota')}{2}F_{i+}(\alpha',\delta',\psi')\right)^2 + \left(\cos(\iota')F_{i\times}(\alpha',\delta',\psi')\right)^2}}{R_i} \tag{6.25}$$

6.1.4. Results from the jump proposal

I have implemented the equations described in Section 6.1.2 as a proposal in a Markov chain Monte Carlo sampling code. I present the effect of including this proposal versus the old proposal including only the sky position and time parameters in Fig. 6.2 for the distance parameter and Fig. 6.3 for the inclination parameter. I injected a known waveform from a non-spinning binary neutron star system ($m_1 = 1.8\,\mathrm{M}_\odot$, $m_2 = 1.6\,\mathrm{M}_\odot$), computed with post-Newtonian expansions, into simulated LIGO and Virgo noise. The MCMC attempts to recover the posterior density using an equivalent frequency-domain template model. In both simulations I started in the reflected extrinsic parameter position with respect to the true position. While the chain using the standard sky reflection proposal (green) gets stuck in the wrong mode, the chain using our improved proposal (blue) instantly finds the correct mode and is able to down-weight the wrong mode by proposing and rejecting jumps towards it. Here the blue distribution is the correct probability density function of the problem, with the dot-dashed red line marking the injection value.

Both cases use parallel tempering with 8 chains each and a maximum temperature of 10.0, which does not help to find the correct mode of the distribution by itself. Other general improvements on the Markov chain Monte Carlo algorithm such as differential evolution require some past samples of the chain to be in the correct location in order to be helpful, and as such will need a proposal akin to the one described here. Both analysis used a physically motivated prior, for instance uniform in inclination and volume. Small distance have then a lower prior value, but the likelihood of the wrong mode at the shorter distance is actually high enough for both modes to have a comparable maximum posterior value (but the correct mode as a greater posterior volume).

This proposal allows for a much better exploration of the extrinsic parameter space for non-spinning gravitational wave signals. It should still be helpful in the spinning case for which leading order effects are equal to the non-spinning case in most occasions. Continuing this work, it may be possible that using an approximation beyond Quadrupole instead of Eq. 6.13 leads to a better handle the spinning case where there is not simple relation between H_+ and $H_\times$. Preliminary investigations have shown correlations between spin parameters and extrinsic parameters due to the precession of the orbital plane in

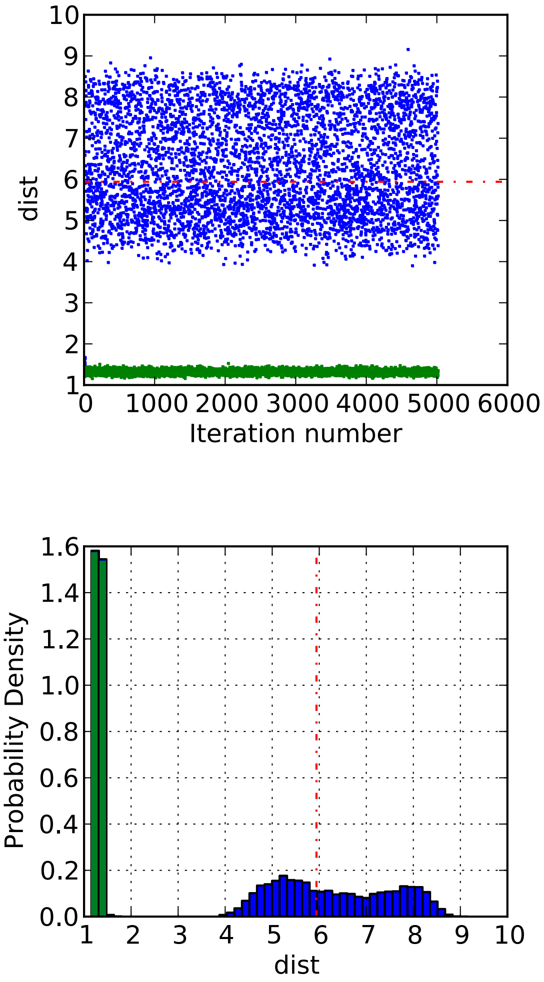

Figure 6.2. Plots of the distance samples from two independent chains as function of iteration number (left panel), using the standard sky reflection proposal (green), and my new proposal (blue) described in Section 6.1.2, and the corresponding sampled distributions (right panel). Both chains start in the wrong mode, see Section 6.1.4. The new proposal enables the chain to find and correctly weight both modes, and eventually sample the probability density function. The dot-dashed red line marks the injection value.

spinning systems. It may then be necessary to include some intrinsic parameters to construct a more efficient proposal for spinning analyses.

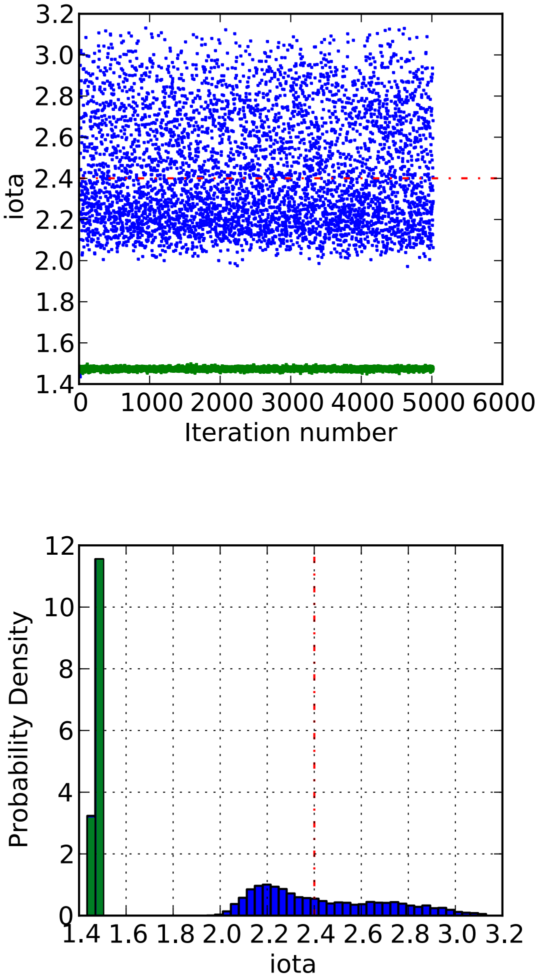

Figure 6.3. Plots of the inclination samples from two independent chains as function of iteration number (left panel), for the standard sky reflection proposal (green), and my new proposal (blue) described in Section 6.1.2, and the corresponding sampled distribution (right panel). Both chains start in the wrong mode, see Section 6.1.4. The new proposal enables the chain to find and correctly weight both modes, and eventually sample the probability density function. The dot-dashed red line marks the injection value.

CHAPTER 7

The power of the Bayes factor to distinguishing between spinning and non-spinning compact binary coalescences

Thanks in part to the work presented in this dissertation, it has now been accepted within the LIGO-Virgo Collaboration that in order to extract astrophysical parameters of source systems in Advanced LIGO/Virgo data, spin effects have to be included when doing parameter estimation analysis. Given the complexity inherent to the high dimensions and strong correlations of the spinning parameter space, one can ask what limits our ability to distinguish non-spinning versus spinning signals. One way to answer this question is to explore when a non-spinning signal becomes indistinguishable from a spinning signal. I am using the Bayesian inference code to compute evidences for non-spinning and spinning models on various injections, and to try to assess the location in parameter space where non-spinning signals can hide.

7.1. Simulation setup

The simulation described in this section consists on injecting a signal with and without spin into synthetic advanced detector noise simulated from two collocated Advanced LIGO detectors in the Hanford site, one Advanced LIGO detector in the Livingston site and one Advanced Virgo detector in the Pisa cite. I then compute the evidence for the spinning model and the non-spinning model by using the same template, fixing the spin parameters to zero. For the work in this section I am using an inspiral-only, post-Newtonian template, with phase effects up to 3.5pN and spin effects included up to 2.5pN using the SpinTaylorT4 approximant (STPN, see table 2.1). It is important for this type of study to use the same template family, as differences such as waveform termination criterions can lead to differences in evidences that would contaminate the difference due to the physical effect I am trying to measure. (For instance, templates generated in the frequency domain on the one hand, and the time domain on the other hand will have by nature different termination criterions and different effective length).

The discriminating power of the Bayes factor in the case of the spinning model versus the non-spinning model ($B_{spin,nospin}$) will depend on the parameters of the signal present in the data. This is a fifteen-dimensional parameter space and in this study I am presenting results on only a few subspaces. The signal injected in the following analysis comes from a binary of masses $m_1 = 8\,\mathrm{M}_{\odot}$ and $m_2 = 4\,\mathrm{M}_{\odot}$. For the spinning injections, the spins are set to $a_1 = 0.7$ and $a_2 = 0.7$, misaligned with the orbital angular momentum by $\vec{S_1} \cdot \vec{L} = \mathrm{tilt1} = 0.85\,\mathrm{rad}$ and $\vec{S_2} \cdot \vec{L} = \mathrm{tilt2} = 0.62\,\mathrm{rad}$. I vary the distance and corresponding signal-to-noise ratio, the inclination of the orbital angular momentum with the line of sight (defined at the beginning of the generated signal, at 30 Hz), and the sky position of this fiducial binary.

7.2. Distinguishing between spin and no spin: results

For a binary system with inclination $\iota = \pi/8\,\mathrm{rad}$ located at $\alpha = 0.65\,\mathrm{rad}$, $\delta = 0.58\,\mathrm{rad}$ at GPS time $t_c = 894383679\,\mathrm{s}$, I computed the Bayes factor of the spinning model versus

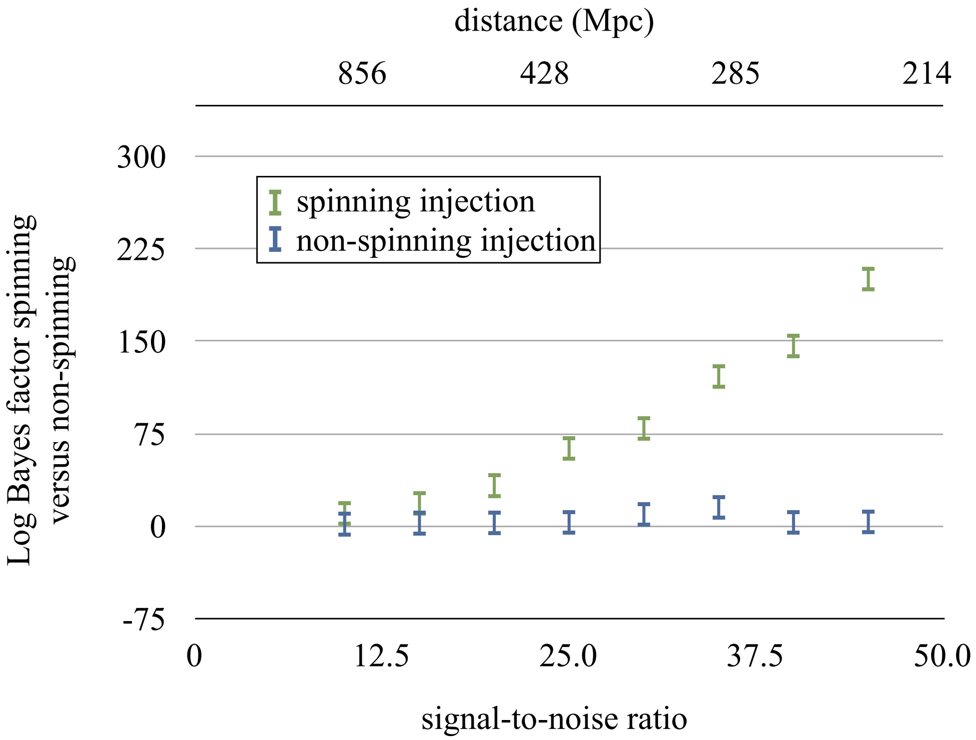

Figure 7.1. Logarithm of the Bayes factor $B_{spin,nospin}$ (Eq. 1.44) of the spinning model versus the non-spinning model as a function of signal-to-noise ratio. Bayes factors are obtained on a non-spinning injection (blue) and the corresponding spinning injection (green), described in Section 7.1. The error bars are obtained by bootstrapping. The inclination is fixed at $\iota = \pi/8\,\mathrm{rad}$.

the non-spinning model varying the distance as a proxy to vary the signal-to-noise ratio. The results are summarised in Fig. 7.1.

In this case, the spinning hypothesis becomes undistinguishable from the spinning hypothesis at a signal-to-noise ratio of about 20. Further investigations at random inclinations and sky positions seem to agree on average with this value, see for instance

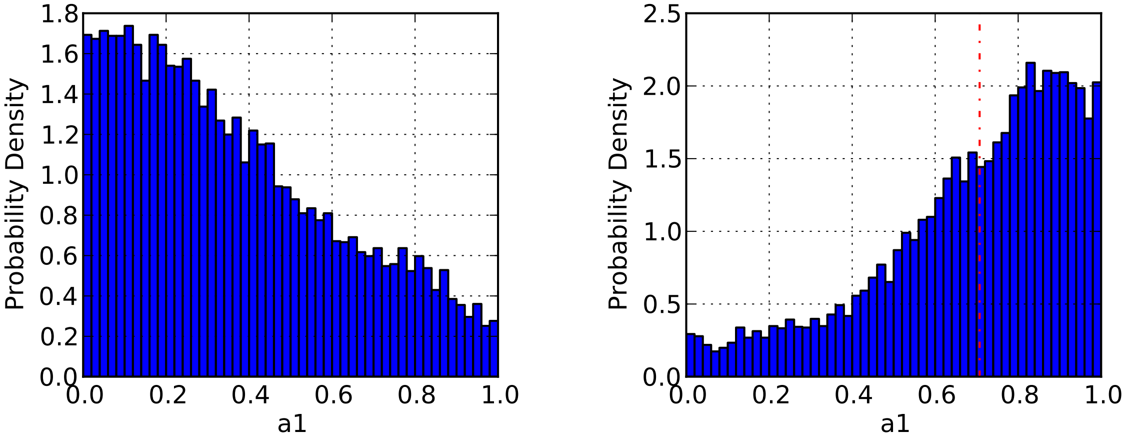

Figure 7.2. Probability density functions for the spin magnitude of the most massive component of the binary a_1, on a non-spinning injection (right) and a spinning injection (left, the injection value is marked by the vertical red dashed line) for the leftmost injections in Fig. 7.1. Even through at this injection signal-to-noise ratio of 10 the Bayes factor cannot distinguish between the spinning and non-spinning hypotheses, the probability density function favours a spin of zero on the non-spinning injection and a significant spin on the spinning injection.

Fig. 7.3. However some special configurations can lower somewhat the threshold, see for instance the inclination in Fig. 7.4. This number is to be compared with what is considered a minimum signal-to-noise ratio threshold of 8 for a detection. Even though for signal-to-noise ratios below 20 the Bayes factor alone cannot distinguish between the two hypotheses, looking at the individual probability density functions in Fig. 7.1 it is possible to get some constraints on the spinning nature of the signal.

A spinning signals sends time-varying amount of power in the two polarisations due to the precession of its orbital plane. The orbital plane of a non-spinning signal is constant. This qualitative difference between the two cases becomes significant as the inclination of the signal gets more and more towards edge-on. (In other words, it is easier to see

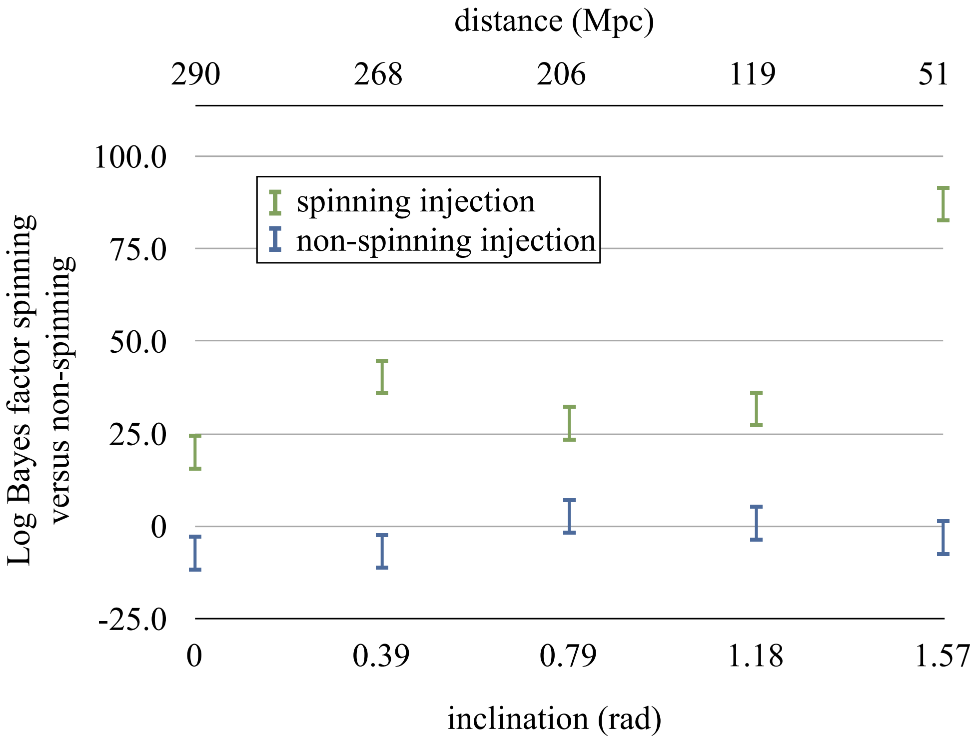

Figure 7.3. Logarithm of the Bayes factor $B_{spin,nospin}$ (Eq. 1.44) of the spinning model versus the non-spinning model as a function of inclination. Bayes factors are obtained on a non-spinning injection (blue) and the corresponding spinning injection (green), described in Section 7.1. The error bars are obtained by bootstrapping. The signal-to-noise ratio is fixed at 20.

if the plane of the orbit is wobbling by seeing it from the side). In Fig. 7.3 I show the logarithm of the Bayes factor as a function of inclination for a fixed signal-to-noise ratio of 20. The distance is scaled down as the inclination increases to keep the signal-to-noise ratio constant.

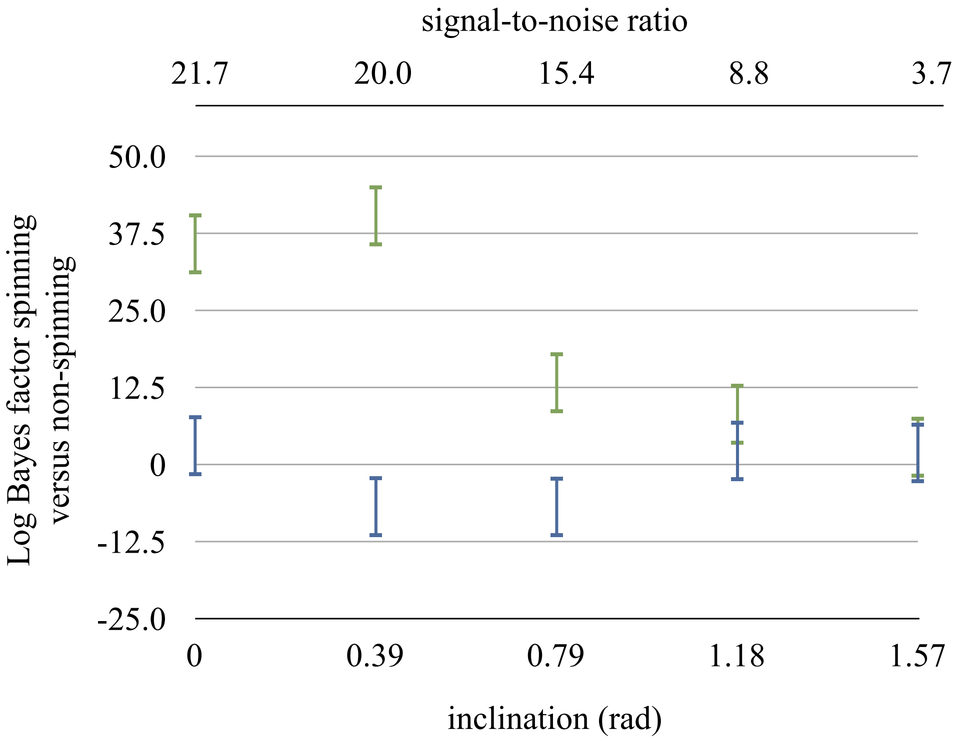

Figure 7.4. Logarithm of the Bayes factor $B_{spin,nospin}$ (Eq. 1.44) of the spinning model versus the non-spinning model as a function of inclination. Bayes factors are obtained on a non-spinning injection (blue) and the corresponding spinning injection (green), described in Section 7.1. The error bars are obtained by bootstrapping. The distance is fixed at $d = 237\,\mathrm{Mpc}$ which results in the signal-to-noise ratio labelled on top of the graph.

The combined effect of the signal-to-noise ratio and inclination are show in Fig. 7.4 where I fixed the distance at $d = 237\,\mathrm{Mpc}$.

As the inclination gets more and more towards edge-on, the signal-to-noise ratio becomes too low for the Bayes factor to distinguish between the spinning and non-spinning models. Additionally, injecting the signal from five different sky locations did not change the Bayes factor beyond the statistical error.

7.3. Conclusion and further work

This work allows to quantify the signal-to-noise ratio cut-off of the Bayes factor discriminating power as a function of inclination. Further studies are needed to get a more accurate estimate. Beyond sampling more densely the parameter space explored in this study, further work should explore the following:

- The effect of merger and ring-down is to be investigated. The spin effects of a waveform are stronger near its end, where the inspiral-only templates used in this study are inaccurate and break down. There are no precessing template with merger and ring-down available at the time of this writing, but recent advances in numerical relativity should remedy this. In addition, since precession seems to be the biggest contributing effect, a single spin analysis may be accurate enough and simpler to execute.
- This analysis should be made on injections of varying masses and spin values. I only did a coarse preliminary investigation with random masses and spin, which was consistent with the findings above, but more complete work is needed.
- In the one detector case, the sky position of the injection matters in order to distinguish spin due the strong asymmetry of the antenna beam pattern [69]. In the case of a three-site network, the overall sensitivity pattern is more spherically symmetric, which may explain the finding in this study that the Bayes factors

can equally well discriminate in five random sky locations. However a denser sky coverage is needed to fully answer this point.

- This investigation was done on ideal, stationary and Gaussian noise. However, as soon as real Advanced LIGO-Virgo noise is available, the robustness of these results has to be verified.

CHAPTER 8

Collaborative projects

The work described in this chapter consists of projects where I had a significant contribution, but I did not lead myself.

8.1. Estimating parameters of coalescing compact binaries with proposed advanced detector networks

One of the goals of gravitational-wave astronomy is simultaneous detection of gravitational-wave signals from merging compact-object binaries and the electromagnetic transients from these mergers. With the next generation of advanced ground-based gravitational wave detectors under construction, I participated in the examination of the benefits of the proposed extension of the detector network to include a fourth site in Australia or India in addition to the network of Hanford, Livingston and Cascina sites. Using Bayesian parameter-estimation analyses of simulated gravitational-wave signals from a range of coalescing-binary locations and orientations, I studied the improvement in parameter estimation. It was found that a fourth detector site can break degeneracies in several parameters; in particular, the localisation of the source on the sky is improved by a factor of 4, with more modest improvements in distance and binary inclination estimates [70]. This enhanced ability to localise sources on the sky will be crucial in any search for electromagnetic counterparts to detected gravitational-wave signals. The study helped the

National Science Foundation deliver an approval of the LIGO South project, in wait of confirmation by the Indian government.

8.2. Sky localisation accuracy of gravitational-wave data analysis

The gravitational-wave detection with the most confidence would very possibly be one accompanied with and electromagnetic counterpart. Intrinsically, gravitational-wave detectors are not pointing instruments and are sensitive to (almost) the entire sky. The best scenario would be a gravitational-wave detection informing electromagnetic observatories where to point, and being able to do so as quickly as possible. A LIGO-Virgo collaboration-wide effort is ongoing trying to understand the tradeoffs between accuracy and speed for several available sky localisation techniques. In particular, Bayesian inference techniques stand at one end of the spectrum, being the slowest but also the most accurate, and hence most practical in identifying hosts galaxies electromagnetically. I am part of a group hoping to quantify the tradeoffs faster methods are making.

8.3. Binary neutron stars, measurements of mass and tidal effects

Double neutron-star systems are of special interest in gravitational-wave astronomy since one can safely ignore their spins (observed values are well below the dynamically interesting spin regime), making detection and parameter estimation easier. Also, accurate neutron-star mass estimates are the first step towards gravitational-waves observations helping to solve the puzzle of neutron-star equation of state. However it is not clear exactly what the most accurate but realistic neutron-star mass measurements and equation-of-state constraints we can get out of the advance detector network are as a function of the signal-to-noise ratio. I am part of the effort trying to answer this question.

8.4. Effects of amplitude correction in gravitational-wave recovery templates

One common approximation in parameter estimation of gravitational waves using post-Newtonian templates is to only compute post-Newtonian expansion terms for the phase of the model template. But one can also compute the proper terms for its amplitude, which can potentially reveal more information from the data, and break degeneracies present in phase-only expansions. Several simulation campaigns are ongoing to estimate the parameter-estimation benefits of including up to 1.5pN corrections in the amplitude of the signal model.

Bibliography

[1] A. Einstein. Approximative Integration of the Field Equations of Gravitation. *Preuss. Akad. Wiss. Berlin*, page 688, 1916.

[2] A. Einstein. Über Gravitationswellen. *Preuss. Akad. Wiss. Berlin*, pages 154–167, 1918.

[3] R. A. Hulse and J. H. Taylor. Discovery of a pulsar in a binary system. *Astroph. J. Lett.*, 195:L51–L53, January 1975.

[4] Curt Cutler and Kip S. Thorne. An overview of gravitational-wave sources. In Nigel T. Bishop and Sunil D. Maharaj, editors, *Proceedings of GR16*. WorldScientific, Singapore, 2002.

[5] B. Abbott and R. Abbott et al. Observation of a kilogram-scale oscillator near its quantum ground state. *New Journal of Physics*, 11(7):073032–+, July 2009.

[6] F. Acernese et al. Virgo status. *Class. Quant. Grav.*, 25(18):184001–+, September 2008.

[7] J. Abadie et al. Predictions for the rates of compact binary coalescences observable by ground-based gravitational-wave detectors. *Class. Quant. Grav.*, 27:173001, March 2010.

[8] V. Raymond, M. V. van der Sluys, I. Mandel, V. Kalogera, C. Röver, and N. Christensen. Degeneracies in sky localization determination from a spinning coalescing binary through gravitational wave observations: a Markov-chain Monte Carlo analysis for two detectors. *Classical and Quantum Gravity*, 26(11):114007, June 2009.

[9] C. Röver, R. Meyer, and N. Christensen. Bayesian inference on compact binary inspiral gravitational radiation signals in interferometric data. *Class. Quant. Grav.*, 23:4895–4906, August 2006.

[10] C. Röver, R. Meyer, and N. Christensen. Coherent Bayesian inference on compact binary inspirals using a network of interferometric gravitational wave detectors. *Phys. Rev. D*, 75(6):062004, March 2007a.

[11] J. Veitch and A. Vecchio. Bayesian approach to the follow-up of candidate gravitational wave signals. *Phys. Rev. D*, 78(2):022001, July 2008.

[12] J. Veitch and A. Vecchio. Assigning confidence to inspiral gravitational wave candidates with Bayesian model selection. *Classical and Quantum Gravity*, 25(18):184010, September 2008.

[13] J. Veitch and A. Vecchio. Bayesian coherent analysis of in-spiral gravitational wave signals with a detector network. Phys. Rev. D, 81(6):062003–+, March 2010.

[14] J. E. McClintock, R. Narayan, S. W. Davis, L. Gou, A. Kulkarni, J. A. Orosz, R. F. Penna, R. A. Remillard, and J. F. Steiner. Measuring the spins of accreting black holes. *Classical and Quantum Gravity*, 28(11):114009, June 2011.

[15] C. Röver, R. Meyer, G. M. Guidi, A. Viceré, and N. Christensen. Coherent Bayesian analysis of inspiral signals. *Class. Quant. Grav.*, 24:607–+, October 2007b.

[16] M. van der Sluys, V. Raymond, I. Mandel, C. Röver, N. Christensen, V. Kalogera, R. Meyer, and A. Vecchio. Parameter estimation of spinning binary inspirals using Markov chain Monte Carlo. *Classical and Quantum Gravity*, 25(18):184011–+, September 2008.

[17] W. R. Gilks, S. Richardson, and D. J. Spiegelhalter. *Markov chain Monte Carlo in practice.* Chapman & Hall/CRC, 1996.

[18] C. W. Misner, K. S. Thorne, and J. A. Wheeler. *Gravitation.* 1973.

[19] Luc Blanchet. Gravitational radiation from post-Newtonian sources and inspiralling compact binaries. *Living Rev. Rel.*, 9:3, 2006.

[20] S. F. Portegies Zwart and S. L. W. McMillan. Black hole mergers in the universe. ApJ, 528:L17, 2000.

[21] M. Kesden, U. Sperhake, and E. Berti. Final spins from the merger of precessing binary black holes. Phys. Rev. D, 81(8):084054, April 2010.

[22] A. Gelman, J. B. Carlin, H. Stern, and D. B. Rubin. *Bayesian data analysis.* Chapman & Hall / CRC, Boca Raton, 1997.

[23] M. A. T. Figueiredo and A. K. Jain. Unsupervised learning of finite mixture models. *IEEE Transactions on pattern analysis and machine intelligence*, 24(3):381–396, 2002.

[24] Y. F. Atchadé and J. S. Rosenthal. On adaptive Markov chain Monte Carlo algorithms. *Bernoulli*, 11(5):815–828, 2005.

[25] K. Hukushima and K. Nemoto. Exchange Monte Carlo Method and Application to Spin Glass Simulations. *Journal of the Physical Society of Japan*, 65:1604, June 1996.

[26] U. Hansmann. Parallel tempering algorithm for conformational studies of biological molecules. *Chemical Physics Letters*, 281:140–150, December 1997.

[27] C. Röver. *Bayesian inference on astrophysical binary inspirals based on gravitational-wave measurements*. PhD thesis, The University of Auckland, 2007. URL `http://hdl.handle.net/2292/2356`.

[28] J. Skilling. Nested sampling for general Bayesian computation. *Bayesian Analysis*, 1(4):833–860, 2006.

[29] Michael A. Newton and Adrian E. Raftery. Approximate bayesian inference with the weighted likelihood bootstrap. *JRSS B*, 56(1):3–48, 1994. `http://www.jstor.org/stable/2346025`.

[30] M. D. Weinberg. Computing the Bayesian Factor from a Markov chain Monte Carlo Simulation of the Posterior Distribution. *ArXiv e-prints*, November 2009.

[31] R. Van Haasteren. Bayesian evidence: can we beat MultiNest using traditional MCMC methods? *ArXiv e-prints*, 0911.2150, November 2009.

[32] J. M. Weisberg, D. J. Nice, and J. H. Taylor. Timing Measurements of the Relativistic Binary Pulsar PSR B1913+16. ApJ, 722:1030–1034, October 2010.

[33] J. Abadie et al. Search for Gravitational Waves from Low Mass Compact Binary Coalescence in LIGO's Sixth Science Run and Virgo's Science Runs 2 and 3. *to be published, Phys. Rev. D*, 2012.

[34] The LIGO Scientific Collaboration, Virgo Collaboration: J. Abadie, B. P. Abbott, R. Abbott, T. D. Abbott, M. Abernathy, T. Accadia, F. Acernese, C. Adams, and R. Adhikari et al. Implementation and testing of the first prompt search for electromagnetic counterparts to gravitational wave transients. *arXiv:1109.3498*, September 2011.

[35] Bloom Joshua S. et al. Astro2010 decadal survey whitepaper: Coordinated science in the gravitational and electromagnetic skies. 2009.

[36] Feryal Ozel, Dimitrios Psaltis, Ramesh Narayan, and Jeffrey E. McClintock. The Black Hole Mass Distribution in the Galaxy. *Astrophys. J.*, 725:1918–1927, 2010.

[37] W. M. Farr, N. Sravan, A. Cantrell, L. Kreidberg, C. D. Bailyn, I. Mandel, and V. Kalogera. The Mass Distribution of Stellar-mass Black Holes. ApJ, 741:103, November 2011.

[38] T. Bulik and K. Belczyński. Constraints on the Binary Evolution from Chirp Mass Measurements. ApJ, 589:L37–L40, May 2003.

[39] I. Mandel and R. O'Shaughnessy. Compact binary coalescences in the band of ground-based gravitational-wave detectors. *Classical and Quantum Gravity*, 27(11):114007, June 2010.

[40] V. Raymond, M. V. van der Sluys, I. Mandel, V. Kalogera, C. Röver, and N. Christensen. The effects of LIGO detector noise on a 15-dimensional Markov-chain Monte Carlo analysis of gravitational-wave signals. *Classical and Quantum Gravity*, 27(11):114009, June 2010.

[41] LSC Algorithm Library.

[42] A. Gelman and D. B. Rubin. Inference from iterative simulation using multiple sequences. *Statistical Science*, 7:457–472, 1992.

[43] Duncan A. Brown. Searching for Gravitational Radiation from Binary Black Hole MACHOs in the Galactic Halo. 2004.

[44] Alessandra Buonanno, Bala R. Iyer, Evan Ochsner, Yi Pan, and B. S. Sathyaprakash. Comparison of post-newtonian templates for compact binary inspiral signals in gravitational-wave detectors. *Phys. Rev. D*, 80(8):084043, October 2009.

[45] Alessandra Buonanno, Yanbei Chen, and Michele Vallisneri. Detecting gravitational waves from precessing binaries of spinning compact objects: Adiabatic limit. *Phys. Rev. D*, 67:104025, 2003. Erratum-ibid. 74 (2006) 029904(E).

[46] J. Abadie et al. Calibration of the LIGO Gravitational Wave Detectors in the Fifth Science Run. *Nucl. Instrum. Meth. A*, 624:223–240, 2010.

[47] S. Vitale, W. Del Pozzo, T. G. F. Li, C. Van Den Broeck, I. Mandel, B. Aylott, and J. Veitch. Effect of calibration errors on Bayesian parameter estimation for gravitational wave signals from inspiral binary systems in the Advanced Detectors era. *ArXiv e-prints*, November 2011.

[48] LIGO Scientific Collaboration and Virgo Collaboration, The LIGO / Virgo Blind Injection GW100916 (2011).

[49] Alessandra Buonanno et al. Toward faithful templates for non-spinning binary black holes using the effective-one-body approach. *Phys. Rev. D*, 76:104049, 2007.

[50] Alessandra Buonanno, Yanbei Chen, and Michele Vallisneri. Detection template families for gravitational waves from the final stages of binary-black-hole inspirals: Nonspinning case. *Phys. Rev. D*, 67:024016, 2003. Erratum-ibid. 74 (2006) 029903(E).

[51] Theocharis A. Apostolatos, Curt Cutler, Gerald J. Sussman, and Kip S. Thorne. Spin-induced orbital precession and its modulation of the gravitational waveforms from merging binaries. *Phys. Rev. D*, 49:6274, 1994.

[52] P. Grandclément, V. Kalogera, and A. Vecchio. Searching for gravitational waves from the inspiral of precessing binary systems: Problems with current waveforms. *Phys. Rev. D*, 67:042003, 2003.

[53] A. Vecchio. LISA observations of rapidly spinning massive black hole binary systems. *Phys. Rev. D*, 70(4):042001, August 2004.

[54] R. N. Lang and S. A. Hughes. Measuring coalescing massive binary black holes with gravitational waves: The impact of spin-induced precession. *Phys. Rev. D*, 74(12):122001, December 2006.

[55] M. V. van der Sluys, C. Röver, A. Stroeer, V. Raymond, I. Mandel, N. Christensen, V. Kalogera, R. Meyer, and A. Vecchio. Gravitational-Wave Astronomy with Inspiral Signals of Spinning Compact-Object Binaries. ApJ, 688:L61–L64, December 2008.

[56] LSC Algorithm Library software packages LAL, LALWRAPPER, and LALAPPS.

[57] P. Fritschel. Second generation instruments for the Laser Interferometer Gravitational Wave Observatory (LIGO). In M. Cruise and P. Saulson, editors, *Society of Photo-Optical Instrumentation Engineers (SPIE) Conference Series*, volume 4856 of *Presented at the Society of Photo-Optical Instrumentation Engineers (SPIE) Conference*, pages 282–291, March 2003.

[58] Lawrence E. Kidder. Coalescing binary systems of compact objects to (post)[sup 5/2]-Newtonian order. v. spin effects. *Phys. Rev. D*, 52(2):821–847, 1995.

[59] Clifford M. Will and Alan G. Wiseman. Gravitational radiation from compact binary systems: Gravitational waveforms and energy loss to second post-Newtonian order. *Phys. Rev. D*, 54:4813–4848, 1996.

[60] Guillaume Faye, Luc Blanchet, and Alessandra Buonanno. Higher-order spin effects in the dynamics of compact binaries. I: Equations of motion. *Phys. Rev.*, D74:104033, 2006.

[61] Luc Blanchet, Alessandra Buonanno, and Guillaume Faye. Higher-order spin effects in the dynamics of compact binaries II. Radiation field. *Phys. Rev.*, D74:104034, 2006.

[62] F. Cavalier, M. Barsuglia, M.-A. Bizouard, V. Brisson, A.-C. Clapson, M. Davier, P. Hello, S. Kreckelbergh, N. Leroy, and M. Varvella. Reconstruction of source location in a network of gravitational wave interferometric detectors. *Phys. Rev. D*, 74(8):082004–+, October 2006.

[63] J. Markowitz, M. Zanolin, L. Cadonati, and E. Katsavounidis. Gravitational wave burst source direction estimation using time and amplitude information. *Phys. Rev. D*, 78(12):122003–+, December 2008.

[64] A. C. Searle, P. J. Sutton, and M. Tinto. Bayesian detection of unmodeled bursts of gravitational waves. *arXiv: gr-qc/0809.2809*, September 2008.

[65] F. Beauville et al. Detailed comparison of LIGO and Virgo inspiral pipelines in preparation for a joint search. *Class. Quantum Grav.*, 25:045001, 2008.

[66] P. Ajith and Sukanta Bose. Estimating the parameters of non-spinning binary black holes using ground-based gravitational-wave detectors: Statistical errors. 2009.

[67] Benjamin Aylott et al. Testing gravitational-wave searches with numerical relativity waveforms: Results from the first Numerical INJection Analysis (NINJA) project. *Class. Quantum Grav.*, 26:165008, 2009.

[68] B. P. Abbott and R. Abbott et al. Search for gravitational waves from low mass binary coalescences in the first year of LIGO's S5 data. Phys. Rev. D, 79(12):122001, June 2009.

[69] D. A. Brown, A. Lundgren, and R. O'Shaughnessy. Nonspinning searches for spinning binaries in ground-based detector data: Amplitude and mismatch predictions in the constant precession cone approximation. *ArXiv e-prints*, March 2012.

[70] J. Veitch, I. Mandel, B. Aylott, B. Farr, V. Raymond, C. Rodriguez, M. van der Sluys, V. Kalogera, and A. Vecchio. Estimating parameters of coalescing compact binaries with proposed advanced detector networks. *ArXiv e-prints*, January 2012.